



HAL
open science

Kinetic Isotopic Degassing of CO₂ During the 2021 Fagradalsfjall Eruption and the $\delta^{13}\text{C}$ Signature of the Icelandic Mantle

Yves Moussallam, Estelle F Rose-koga, Tobias P Fischer, Guillaume Georgeais, Hyun Joo Lee, Janine Birnbaum, Melissa A Pfeffer, Talfan Barnie, Edouard Regis

► To cite this version:

Yves Moussallam, Estelle F Rose-koga, Tobias P Fischer, Guillaume Georgeais, Hyun Joo Lee, et al.. Kinetic Isotopic Degassing of CO₂ During the 2021 Fagradalsfjall Eruption and the $\delta^{13}\text{C}$ Signature of the Icelandic Mantle. *Geochemistry, Geophysics, Geosystems*, 2024, 25 (12), 10.1029/2024GC011997. insu-04849021

HAL Id: insu-04849021

<https://insu.hal.science/insu-04849021v1>

Submitted on 19 Dec 2024

HAL is a multi-disciplinary open access archive for the deposit and dissemination of scientific research documents, whether they are published or not. The documents may come from teaching and research institutions in France or abroad, or from public or private research centers.

L'archive ouverte pluridisciplinaire **HAL**, est destinée au dépôt et à la diffusion de documents scientifiques de niveau recherche, publiés ou non, émanant des établissements d'enseignement et de recherche français ou étrangers, des laboratoires publics ou privés.



Distributed under a Creative Commons Attribution - NonCommercial - NoDerivatives 4.0 International License

Geochemistry, Geophysics, Geosystems[®]



RESEARCH ARTICLE

10.1029/2024GC011997

Key Points:

- First concurrent measurements of $\delta^{13}\text{C}$ in melt inclusions and volcanic gases
- Kinetic isotopic degassing of CO_2 during magma ascent during the 2021 Fagradalsfjall eruption
- $\delta^{13}\text{C}$ signature of the Icelandic mantle constrained to $-6.5 \pm 2.5\text{‰}$

Supporting Information:

Supporting Information may be found in the online version of this article.

Correspondence to:

Y. Moussallam,
yves.moussallam@ldeo.columbia.edu







Citation:

Moussallam, Y., Rose-Koga, E. F., Fischer, T. P., Georgeais, G., Lee, H. J., Birnbaum, J., et al. (2024). Kinetic isotopic degassing of CO_2 during the 2021 Fagradalsfjall eruption and the $\delta^{13}\text{C}$ signature of the Icelandic mantle. *Geochemistry, Geophysics, Geosystems*, 25, e2024GC011997. <https://doi.org/10.1029/2024GC011997>

Received 28 OCT 2024

Accepted 19 NOV 2024

Kinetic Isotopic Degassing of CO_2 During the 2021 Fagradalsfjall Eruption and the $\delta^{13}\text{C}$ Signature of the Icelandic Mantle

Yves Moussallam¹ , Estelle F. Rose-Koga² , Tobias P. Fischer³ , Guillaume Georgeais¹, Hyun Joo Lee¹ , Janine Birnbaum^{1,4} , Melissa A. Pfeffer⁵ , Talfan Barnie⁵, and Edouard Regis⁶

¹Lamont-Doherty Earth Observatory, Columbia University, New York, NY, USA, ²ISTO, UMR 7327, Université d'Orléans–CNRS–OSUC, Orléans cedex 2, France, ³Department of Earth and Planetary Sciences, University of New Mexico, Albuquerque, NM, USA, ⁴Ludwig-Maximilians-Universität München, München, Germany, ⁵Icelandic Meteorological Office, Reykjavík, Iceland, ⁶Observatoire de Physique du Globe de Clermont Ferrand (OPGC), Aubière, France

Abstract CO_2 is the first volatile to exsolve in magmatic systems and plays a crucial role in driving magma ascent and volcanic eruptions. Carbon stable isotopes serve as valuable tracers for understanding the transfer of CO_2 from the melt to the gas phase during passive degassing or active eruptions. In this study, we present $\delta^{13}\text{C}$ measurements from the 2021 Fagradalsfjall eruption, obtained from (a) volcanic gases emitted during the eruption and collected via unmanned aerial systems (UAS), and (b) a series of mineral-hosted melt inclusions from the corresponding tephra deposits. These data sets jointly track the carbon isotopic evolution of the melt and gas phases during the last 10 km of magma ascent. The isotopic evolution of both phases indicates that kinetic degassing, a process previously only identified in mid-ocean ridge basalts, took place in the 10 to 1 km depth range, followed by equilibrium degassing at near-surface conditions in the last kilometer. Postulating that the melt was first saturated with CO_2 at 27 km depth and that degassing from then to 10 km depth took place via equilibrium isotopic fractionation, the melt inclusion data constrain the initial $\delta^{13}\text{C}$ signature of the Icelandic mantle to $-6.5 \pm 2.5\text{‰}$ but also show indications of possible isotopic heterogeneity in the mantle source.

1. Introduction

Carbon dioxide is a ubiquitous volatile element in magmatic systems on Earth. As the first major volatile species to separate, at depth, into a gaseous phase, understanding its stable isotope systematics and evolution has the capability to provide insights into the complete degassing process. Studies of stable isotopes of CO_2 in natural magmatic systems have been divided into two distinct categories. The first category has focused on volcanic gases, with the $\delta^{13}\text{C}$ in gases emitted from active volcanoes long been used to infer gas origin (e.g., Sano & Marty, 1995; Sano & Williams, 1996; Varekamp et al., 1992). Most of these measurements have been performed on low temperature systems (e.g., Capasso et al., 2005; Chiodini et al., 2011; Hilton et al., 2010; Obase et al., 2022; Sato et al., 2002) as isotopic measurements in gases collected at magmatic temperatures are rare and challenging (e.g., Allard, 1979; Allard et al., 1977; Gerlach & Taylor, 1990). Recent advances in in situ isotope ratio infrared spectroscopy have since allowed $\delta^{13}\text{C}$ measurements in volcanic plumes emitted from the main vent of active volcanoes (e.g., D'Arcy et al., 2022; Fischer et al., 2024; Galle et al., 2021; Liu et al., 2020; Malowany et al., 2017; Rizzo et al., 2014, 2015; Schipper et al., 2017). The second category of studies has focused on erupted lavas, mainly from submarine settings, with $\delta^{13}\text{C}$ measurements performed on CO_2 dissolved in the glass and/or trapped in vesicles (e.g., Aubaud et al., 2004, 2005, 2006; Cartigny et al., 2001; Des Marais & Moore, 1984; Jendrzewski, 1994; Marty & Jambon, 1987; Moore et al., 1977; Pineau et al., 1976; Pineau & Javoy, 1983; Pineau & Javoy, 1994).

In this study, we combine the approaches of both categories. We present $\delta^{13}\text{C}$ measurements on volcanic gases emitted during the 2021 Fagradalsfjall eruption, collected directly above the vent during spattering and effusive activities by an unmanned aerial vehicle (UAV) equipped with an automated gas sampler. We also present $\delta^{13}\text{C}$ measurements in mineral-hosted melt inclusions from tephra erupted during the same event. Our findings reveal evidence for kinetic degassing of CO_2 during magma ascent from 10 to 1 km, followed by equilibrium and/or open-system degassing near the surface in the last kilometer. The results highlight the inappropriateness of utilizing $\delta^{13}\text{C}$ in volcanic gases as a direct indicator of volatile origin without considering the degassing process

and demonstrate the effectiveness of combined-approach investigations in interpreting the intricate process of magma degassing during volcanic eruptions. Our results also suggest that kinetic CO₂ degassing during magma ascent may be more common than previously thought. Furthermore, assuming that degassing at >10 km depth took place via equilibrium isotopic fractionation, we constrain the C isotopic signature of the mantle source beneath the Reykjanes Peninsula to between −4 and −9‰ and show that this source might be locally heterogeneous.

2. Samples and Methods

2.1. The 2021 Fagradalsfjall Eruption

The 2021 Fagradalsfjall eruption of olivine tholeiite basalts on Iceland's Reykjanes Peninsula was preceded by more than a year of volcano–tectonic unrest and began on 19 March 2021 (e.g., Barsotti et al., 2023; Sigmundsson et al., 2022). The first 6 weeks of the eruption were characterized by the formation of multiple vents with spattering activity, followed by mostly effusive and fire fountaining activity from a single crater for the remainder of the eruption. The eruption lasted for 6 months until September 18, 2021, and produced a total of $150 \pm 3 \times 10^6$ m³ of lava flows, of 30 m mean thickness, covering an area of 4.8 km² (Pedersen et al., 2022). Fire fountaining at the main vent oscillated between periodic and non–periodic intervals (Scott et al., 2023) producing gas plumes up to 4 km high (Barnie et al., 2023).

The petrology of the 2021 Fagradalsfjall eruption has been studied in detail by Halldórsson et al. (2022). Focusing on the early phase of the eruption (21 March to 6 May 2021), they characterized the lava as olivine tholeiite basalts with a chemical composition typical of historical Reykjanes Peninsula eruptions. The MgO content ranged from 8.8 to 10.0 wt.% in the whole rock, from 7.6 to 12.3 wt.% in the melt inclusions and from 6.7 to 9.0 wt.% in the matrix glasses. The olivine crystals (up to a few mm in size) have core compositions ranging from Fo₈₂ to Fo₉₀ and rim compositions ranging between Fo₈₀ and Fo₈₈, while plagioclase and clinopyroxene compositions extend similarly to primitive values (An₉₁ and Mg# up to 89, respectively). These characteristics, together with pressure estimates (from melt inclusions volatile content and mineral–melt thermobarometers), all point to a mantle melt directly sourced from the mantle. In detail, Halldórsson et al. (2022) determined that the eruption was mainly sourced from a near-Moho magma reservoir at a depth of more than 15 km but that the earliest phase of erupted magma (March 2021) was dominantly equilibrated at shallow crustal depths (<8 km), while later phases (from 28 April 2021 onwards) were dominantly last equilibrated at deeper (~20, potentially down to 25 km) levels. Concomitant with the deepening of the magma source region with time, the authors also identify an enrichment in trace elements (K₂O/TiO₂, La/Yb and ²⁰⁶Pb/²⁰⁴Pb ratios) over that time interval, indicating the contribution of several eruptible batches of basaltic magmas from a compositionally heterogeneous mantle. Olivine and Plagioclase diffusion chronometry study by Kahl et al. (2022) showed that the magmatic system was mobilized and started traversing the crust in the weeks and days prior to eruption.

2.2. Volcanic Gas Collection by Unmanned Aerial System (UAS)

Three volcanic gas samples were collected, one on 28 June 2021 and two on 01 July 2021, during phase IVa in Barsotti et al. (2023), a time period characterized by less sustained activity with few hours to few days intervals between lava effusion. Samples were collected using an automatic volcanic plume sampler. The gas sampler, designed and assembled at the Observatoire de Physique du Globe de Clermont Ferrand, was mounted on a DJI Matrice 210 UAV and connected to a Tedlar® gas sample bag (Figure 1). The sample apparatus was equipped with an SO₂ sensor and a pump. The SO₂ sensor was read in real time and used to trigger the pump when measured levels exceeded a threshold set between 10 and 50 ppm SO₂. The pump was stopped when the bag pressure exceeded a threshold set between 60 and 200 hPa above the background. Data were also transmitted by radio in real time with an option for the user to start the pump remotely. Four attempts were made to collect gas samples, three of which were successful (the first gas collection attempted on 28 June overfilled and ruptured the Tedlar® bag). On both days the gas samples were acquired while the unmanned aerial system (UAS) was flown directly above the vent. At the time of collection, the vent was open with continuous degassing and low-level bubble bursting activity (Figure 1).

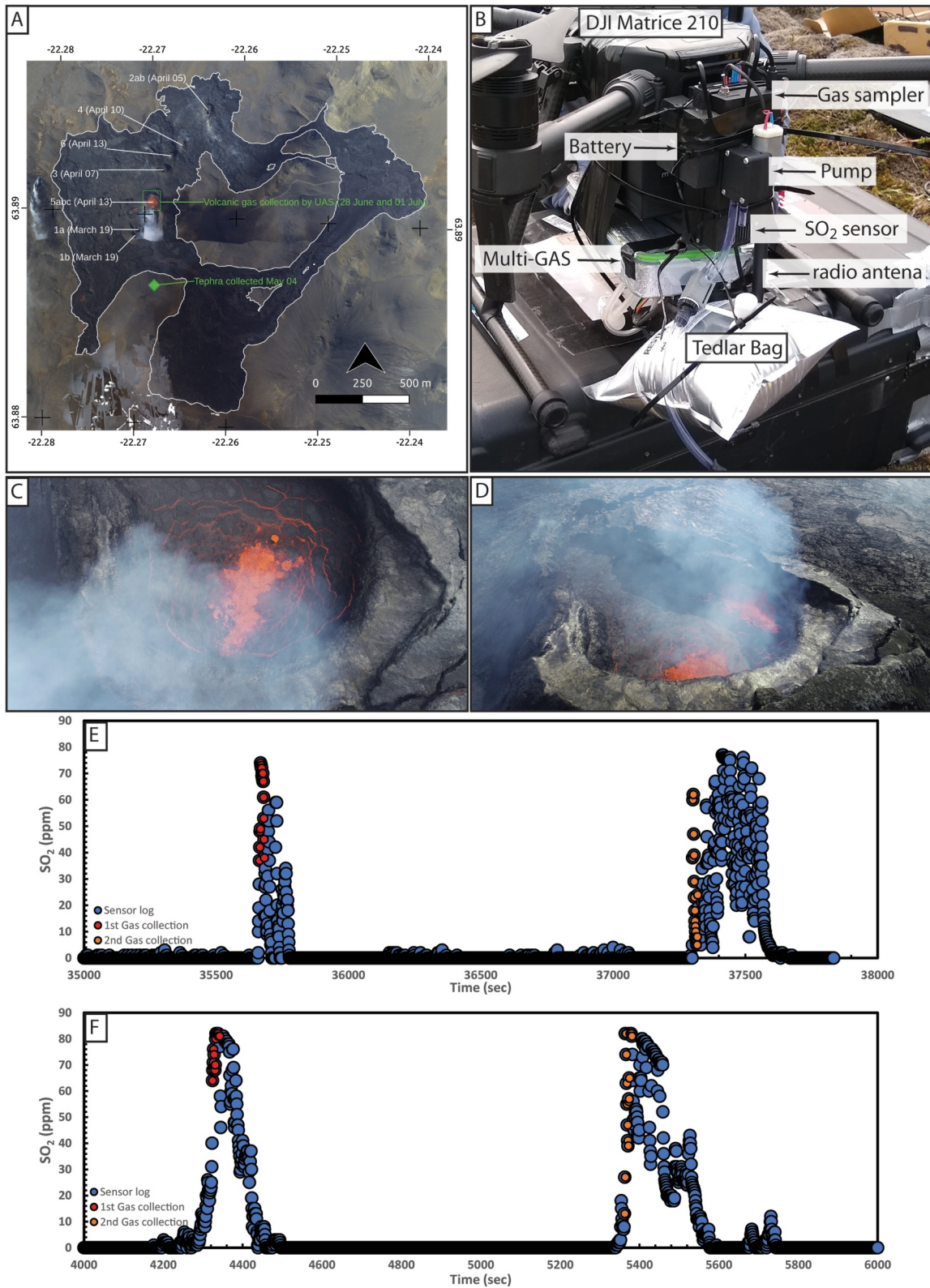


Figure 1.

2.3. Gas $\delta^{13}\text{C}$ Analysis by IR Spectrometry

The $\delta^{13}\text{C}$ values and the CO_2 concentrations of the samples were obtained using a Delta Ray Isotope Ratio Infrared Spectrometer (IRIS) located in the Volatiles Lab at the University of New Mexico. The analytical techniques used were identical to those reported previously (Fischer & Lopez, 2016; Galle et al., 2021; Liu et al., 2020). The error in the $\delta^{13}\text{C}$ analyses is $<0.1\%$ and for CO_2 concentrations <10 ppm.

2.4. Tephra Sample Collection and Preparation

Tephra samples were collected on 04 May 2021 at the lat. 63.8858 long -22.2695 (Figure 1f). Tephra fall had started at this location on 02 May 2021 and was ongoing at the time of collection (Figure 2), so our samples represent material erupted from May 02 to 04 2021. At that time, the activity had already focused on a single vent with pulsating lava fountaining activity (Figure 2; Phase IIIb in Barsotti et al., 2023). Tephra samples were glassy with few olivine phenocrystals and lapilli in size with most fragments smaller than 2 cm.

Samples were crushed and sieved, and crystals of olivine and spinel that were unbroken and contained melt inclusions were selected manually using a binocular microscope (within the grain size range of 0.5–2 mm). The melt inclusions were exposed by individually polishing single crystals. The polishing process was carried out without the use of diamond paste to completely avoid any potential carbon contamination during subsequent ion probe analysis. Instead, after the silicon carbide mats were used for coarse polishing, corundum mats were used for the final stages of polishing with particle sizes of 3 μm , 1 μm , and $\frac{1}{4}$ μm . The individual crystals were then mounted in indium for analysis by secondary ion mass spectrometry (SIMS). The melt inclusions are entirely glassy, 30–130 μm in size and only one contained a retraction bubble occupying $<1\%$ vol (Figures 2 and S1 in Supporting Information S1). Two additional melt inclusions from tephra collected on 04 April 2021 (Phase IIa in Barsotti et al., 2023) were also included for analysis, one of which contained a retraction bubble.

2.5. $\delta^{13}\text{C}$ Analysis in Melt Inclusions by SIMS

Carbon isotopes and CO_2 concentrations were determined utilizing a Cameca IMS 1270 ion microprobe at CRPG–CNRS–Nancy, France, following the procedure of Lee, Moussallam, Rose-Koga, et al. (2024). We utilized a Cs^+ primary beam with a current of 1–3 nA and a 10 kV potential. Depending on the intensity of the signals on the standards and samples, the primary intensity was adjusted to uphold the signal of ^{13}C in the electron multiplier detector (i.e., $<300,000$ cts/s). The area for analysis was selected away from any cracks or gaps on the surface of the sample. A 120 s pre-sputter with a 15×15 μm square raster was applied, and then analyses were performed on the 10 μm spot in the center of the rastered clean area. Secondary negative ions ^{12}C and ^{13}C were detected by an axial electron multiplier (EM) using a magnetic peak switching method. ^{18}O was collected in a Faraday cup (in FC2). We used mass 11.8 for the background measurement of the EM and mass 17.8 for the background measurement of the FC. The counting times were 4 s (EM background), 4 s (^{12}C), 20 s (^{13}C), 4 s (FC2 background) and 2 s (^{18}O). The wait times between the masses were 3, 1, 1, 1 and 1 s, respectively, and a dead time correction of 89 ns was applied. For each measurement, 30 cycles were collected, so each analysis took about 30 min. Using the analytical conditions in Table S1 in Supporting Information S1, the mass resolving power (MRP) was 5000, which is sufficient to discriminate mass ^{13}C from mass $^{12}\text{C}^1\text{H}$. Instrument mass fractionation was characterized using a series of 11 synthetic and one natural mid-ocean ridge basalts (MORB) standards described in Lee, Moussallam, Rose-Koga, et al. (2024) (Figure S2 in Supporting Information S1). CO_2 concentration was determined using the $^{12}\text{C}/^{18}\text{O}$ ratio and known concentrations in standards (Figure S2 in Supporting Information S1).

Figure 1. Gas sample collection by UAS during the 2021 Fagradalsfjall eruption. (a) Map showing the location of the plume sampling and tephra collection sites. Orthoimage base layer and lava outline are derived from an aerial survey conducted on 3rd May 2021 (Pedersen et al., 2022, data available from <https://zenodo.org/records/6598466>). Vents are labeled in accordance with Barsotti et al., 2023. (b) Photograph of the gas sampler mounted on a DJI Matrice 210 drone taken on 28 June 2021. (c, d) Aerial photographs of the vent and gas plume sampled on 28 June 2021. The crater rim is 100 m in diameter. (e, f) time series of SO_2 measured by the gas sampler during flights above the vent on 28 June 2021 and 01 July 2021, respectively. The SO_2 measurements during sample bag filling periods are shown in red and orange.

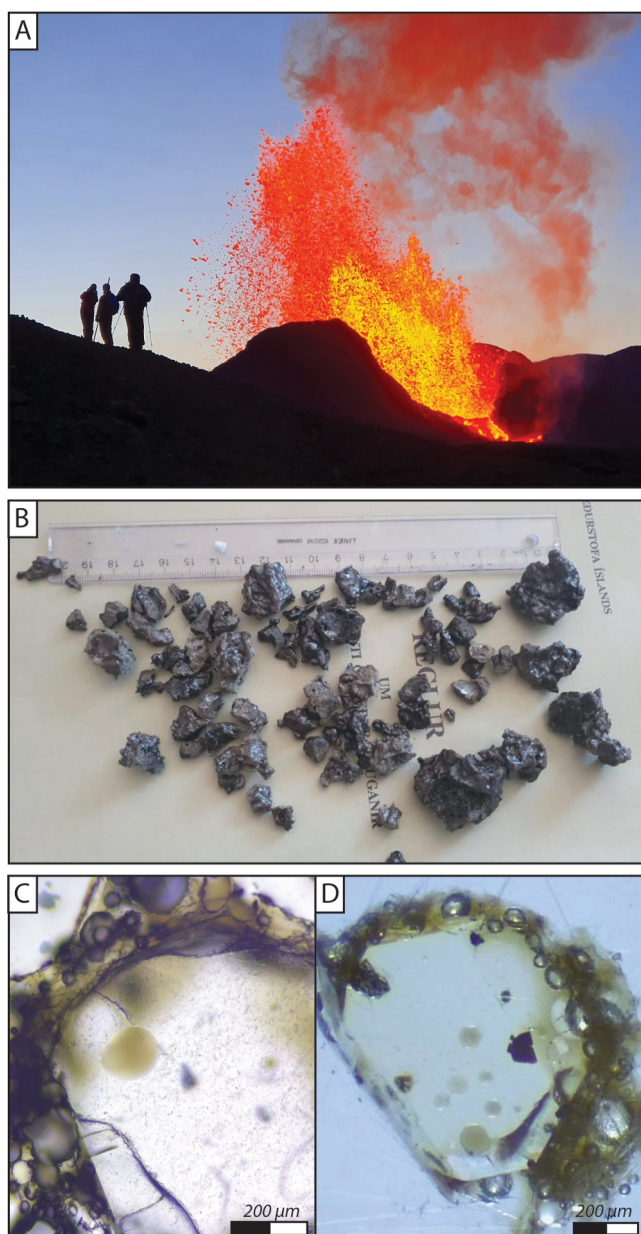


Figure 2. Tephra sample collection during the 2021 Fagradalsfjall eruption. (a) Photograph of the vent and tephra fall produced by fire fountaining activity on 04 May 2021 (fire fountain in this photograph reach ~100 m above the crater floor but heights in excess of 150 m were recorded that day). (b) Photograph of the scoria samples collected on 04 March 2021. (c, d) Olivine crystals containing melt inclusions originating from 04 April and 04 May tephra, respectively.

2.6. Major Element Analysis by EMPA

The major element composition of melt inclusions, their host crystal and the matrix glass surrounding the crystals were measured using a Cameca Sx Five Tactis at the American Museum of Natural History (AMNH) in New York. The instrument was calibrated on mineral standards and glass: Albite (Na, Al), Orthoclase (K, Si), San Carlos olivine (Fe, Mg), Berlinite (P), Anorthite (Ca), TiO₂ (Ti), Rhodon (Mn), Scapolite (Cl) and VG2 (S). For the crystalline phase, beam conditions were set at 15 kV and 10 nA, except for Na and K (both at 4 nA). Peak counting times were 10s for Na and 20s for all other elements. The beam size was set to 1 μm. We measured the host crystal composition by either achieving core to rim transects of host spinel and olivine with a spatial resolution smaller than 15 μm or by doing multiple points next to the MIs, and both at the center and the rim of the host crystals. For the melt inclusions and matrix glass, beam conditions were set at 15 kV and 10 nA, except for Na, K, S and Cl (4, 4, 40 and 40 nA, respectively). Peak counting times were 10s for Na, 30 s for Cl, 60 s for S, and 20s for all other elements. The beam size was set to 10 μm. Sodium was measured first in all analyses to limit the effects of Na loss.

The amount of post-entrapment crystallization (PEC) for olivine-hosted inclusions was estimated using the Petrolog3 software (Danyushevsky & Plechov, 2011). Calculations were performed using the olivine-melt model of Danyushevsky et al. (2000), the density model of Lange and Carmichael (1987), the melt oxidation model of Kress and Carmichael (1988) and the model of Toplis (2005) for the compositional dependence of the olivine-liquid Fe-Mg exchange coefficient (Kd). Calculations were performed assuming a system buffered at $Fe^{3+}/\sum Fe = 0.16$ based on unpublished X-ray absorption near-edge structure (XANES) spectroscopy at the iron K-edge carried out on melt inclusions from the same eruption (during the same session and using the same analytical procedure as described in Moussallam et al., 2023). Note that calculations in Petrolog3 are performed under anhydrous conditions at 1 atm. The resulting PEC estimates ranged from -2.5% to -0.6% with an average of -1.6% and a standard deviation of ±0.7%.

3. Results

3.1. Gas δ¹³C Analysis by IR Spectrometry

Background isotopic measurements and CO₂ concentrations in air free of any volcanic CO₂ were taken from the NOAA global monitoring station at Storrhofdi (flask data from 06 July 2021 analyzed by mass spectrometry by NOAA Global Monitoring Laboratory at University of Colorado/INSTAAR Stable Isotope Laboratory. <https://gml.noaa.gov/>), the southernmost point of Heimaey Island (112 km from the eruption site). Results from IRIS analyses of our gas samples are presented in Table 1. Our plume samples represent variable amounts of mixing between background air and pure volcanic gas. Their total CO₂ content ranged from 515 to 595 ppm CO₂, while the background air contained 412 ppm CO₂. This means that 103–183 ppm CO₂ in our

samples was volcanic, which is consistent with the quantity we would have predicted given the SO₂ amounts at the times of collection (Figure 1) and a CO₂/SO₂ ratio of about 2.4 (Halldórsson et al., 2022). Using the Keeling-plot approach (Keeling, 1958), our δ¹³C and CO₂ abundance data show mixing between ambient air CO₂ and pure volcanic CO₂. We estimate the isotope composition of volcanic CO₂ by determining the y-intercept and associated error of a linear best-fit of δ¹³C versus 1/CO₂ (Figure 3) and obtain a δ¹³C_{volc} of 0.1 ± 1.2‰ (all δ¹³C values given relative to Pee Dee Belemnite).

Table 1
Results From IRIS Analysis of Gas Samples From the 2021 Fagradalsfjall Eruption and Background Air Measurements Taken From NOAA GML Storhofdi Station (<https://gml.noaa.gov/>)

| Sample | Collection date | $\delta^{13}\text{C}$ (‰) | CO ₂ (ppm) |
|--|-----------------|---------------------------|-----------------------|
| Fagra 1 | 28/06/2021 | -7.3 | 515 |
| Fagra 2 | 01/07/2021 | -6.4 | 550 |
| Fagra 3 | 01/07/2021 | -5.7 | 595 |
| Background Air (NOAA, Storhofdi station) | 06/07/2021 | -8.5 | 412 |

Note. Error on $\delta^{13}\text{C}$ is $< 0.1\text{‰}$ (1σ).

3.2. $\delta^{13}\text{C}$ Analysis in Melt Inclusions by SIMS

SIMS results are provided in Table 2 with raw values provided in Table S2 in Supporting Information S1. A total of 11 melt inclusions were analyzed, three of which were large enough for three replicate analyses to be performed each time. Melt inclusion CO₂ content ranged from 1,200 to 400 ppm and $\delta^{13}\text{C}$ values ranged from $-11 \pm 1.3\text{‰}$ to $-2 \pm 1.2\text{‰}$ (1σ). Although analytical errors and scatter are significant, the two melt inclusions with the lowest CO₂ contents (one of which was analyzed three times) also have the highest $\delta^{13}\text{C}$ values (Figure 4). We note that nine out of the 11 melt inclusions analyzed do not contain a shrinkage bubble, hence their CO₂ content and isotopic value cannot have been modified by post-entrapment diffusion into a shrinkage bubble.

3.3. Major Element Analysis by EMPA

EMPA results are provided in Table 3 (Melt inclusions and matrix glasses), Table S3 in Supporting Information S1 (PEC-corrected melt inclusions), Table 4 (olivine and spinel) and Table S4 in Supporting Information S1 (core to rim olivine transect). A total of 11 melt inclusions and their host crystals were analyzed, and three melt inclusions were large enough for two to three replicate analyses to be performed. Further 26 analyses of matrix glasses surrounding the crystals were performed and five core-to-rim transects were performed in olivine host crystals. Figure 5 shows the melt inclusion and matrix glass compositions. On average, the matrix glasses tend to have slightly lower SiO₂ (49.2 ± 0.5 wt.%), and CaO (12.9 ± 0.2 wt.%) contents than the melt inclusions (50.4 ± 0.6 and 13.4 ± 0.2 wt.% respectively, all error reported as one standard deviation), similar MgO contents (8.2 ± 0.3 wt.%) and higher FeO (9.5 ± 0.3 wt.% compared to 8.4 ± 0.5 wt.%) and Na₂O + K₂O contents (2.2 ± 0.1 wt.% compared to 1.8 ± 0.1 wt.%). Most notably the matrix glasses tend to have on average higher K₂O/TiO₂ (0.23 ± 0.02) compared to the melt inclusion (0.09 ± 0.06), although one melt inclusion also records a K₂O/TiO₂ ratio of 0.23.

Host olivine crystals have compositions ranging from Fo_{85.4} to Fo_{88.3} with an average of Fo₈₇. Major element concentration profiles are shown in Figure S3 in Supporting Information S1. Two show normal zoning, one shows no variation (safe for a single point) and two show slight reverse zoning. In four out of five cases, the compositional variations are smaller than 1% in Forsterite content. As expected for near equilibrium melt inclusion–host pairs, there is a clear correlation between the olivine and melt-inclusion compositions (Figure 5d). The average matrix glass composition would be in equilibrium with Fo_{85.5} olivine (based on the same petrolog3 modeling as described for PEC calculations), which is similar to the lowest Fo value we measured on one of the olivine rims (Fo_{85.4}).

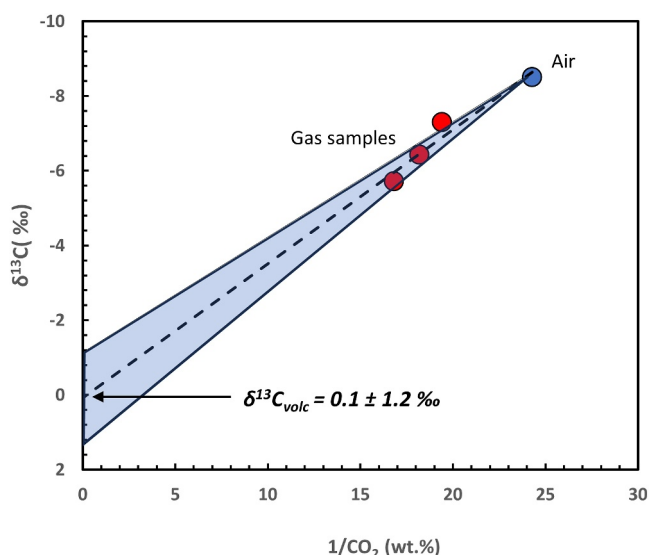


Figure 3. $\delta^{13}\text{C}$ versus $1/\text{CO}_2$ in our gas samples from the 2021 Fagradalsfjall eruption and in local background air (background air values from <https://gml.noaa.gov/>). Dashed line shows the linear best-fit, which intercepts the y-axis at the pure volcanic CO₂ endmember. The blue shaded region shows the 1 sigma error on the extrapolation. Errors on $\delta^{13}\text{C}$ are smaller than the symbols.

4. Discussion

4.1. Isotopic Fractionation During Degassing

The CO₂ content in our melt inclusions, ranging from 1,300 to 400 ppm (corresponding to entrapment pressures of 270 to 97 MPa, entrapment depth

Table 2
Results From SIMS Analysis of Melt Inclusions

| Melt inclusion | Number of analyses | $\delta^{13}\text{C}$ (‰) | 1 sigma error | CO_2 (ppm) | 1 sigma error |
|----------------|--------------------|---------------------------|---------------|---------------------|---------------|
| G404_12 | 3 | -10.2 | 1.6 | 814 | 38 |
| G404_7 | 1 | -9.0 | 1.2 | 1,212 | 56 |
| ICEYT_6a | 1 | -5.8 | 0.9 | 1,309 | 60 |
| ICEYT_6b | 1 | -5.2 | 1.2 | 1,117 | 52 |
| ICEYT_3 | 3 | -4.4 | 0.5 | 386 | 18 |
| ICEYT_8 | 3 | -5.3 | 0.8 | 1,292 | 60 |
| ICEYT_7 | 1 | -11.1 | 1.3 | 1,128 | 52 |
| ICEYMI_3a | 1 | -9.5 | 1.2 | 1,017 | 47 |
| ICEYMI_3b | 1 | -6.7 | 1.4 | 665 | 31 |
| ICEYT_2a | 1 | -2.0 | 1.2 | 425 | 20 |
| ICEYT_2b | 1 | -9.5 | 1.3 | 1,308 | 60 |

Note. For analyses on which repeat measurements were performed, the average $\delta^{13}\text{C}$ value and CO_2 concentrations are reported and the 1 sigma error on the $\delta^{13}\text{C}$ value is the standard deviation on the repeat analysis.

of ~10 to 3.5 km), is within the range found in previous studies of the 2021 Fagradalsfjall eruption (2000 and 100 ppm for most of the inclusions in Halldórsson et al., 2022 who also report one inclusion with 5,000 ppm). CO_2 degassing can occur in four different modes depending on (a) whether the gas phase remains in the system or escapes (closed vs. open system degassing) and (b) whether the diffusion of CO_2 from the melt into the gas bubble is time-limited (equilibrium vs. kinetic degassing) (e.g., Aubaud, 2022; Barry et al., 2014; Brown et al., 1985; Gerlach & Taylor, 1990; Macpherson et al., 2010; Macpherson & Matthey, 1994; Pineau & Javoy, 1994).

For closed system equilibrium degassing (also called batch degassing), the evolution of the melt $\delta^{13}\text{C}$ is given by

$$\delta^{13}\text{C}_{\text{melt}} = \delta^{13}\text{C}_{\text{initial}} - (1 - F) 1000 \ln \alpha_{\text{gas-melt}} \quad (1)$$

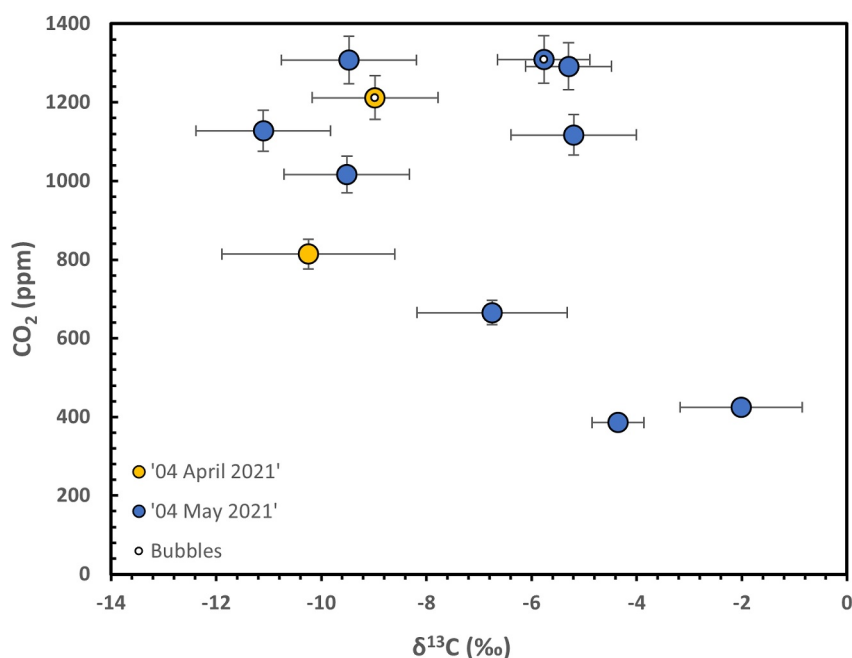


Figure 4. CO_2 content versus $\delta^{13}\text{C}$ for melt inclusions from the 2021 Fagradalsfjall eruption. Inclusions containing a shrinkage bubble are marked with a white dot in their center. Error bars are 1σ .

Table 3
Major Element Composition of Melt Inclusions and Matrix Glasses

| | Number of analyses | SiO ₂ | TiO ₂ | Al ₂ O ₃ | FeO | MnO | MgO | CaO | Na ₂ O | K ₂ O | P ₂ O ₅ | SO ₂ | Cl | Total |
|------------------------|--------------------|------------------|------------------|--------------------------------|------|-----|-----|------|-------------------|------------------|-------------------------------|-----------------|-----|-------|
| Melt inclusions | | | | | | | | | | | | | | |
| Olivine hosted | | | | | | | | | | | | | | |
| G404_12 | 1 | 49.2 | 1.0 | 14.9 | 9.4 | 0.2 | 7.8 | 13.3 | 1.8 | 0.24 | 0.12 | 1,988 | 159 | 98.3 |
| G404_7 | 3 | 50.2 | 0.7 | 15.2 | 8.6 | 0.2 | 8.2 | 13.2 | 1.8 | 0.11 | 0.08 | 1,505 | 39 | 98.3 |
| ICEYT_6a | 1 | 50.2 | 0.6 | 15.4 | 8.8 | 0.2 | 8.5 | 13.6 | 1.7 | 0.03 | 0.08 | 1,204 | 48 | 99.0 |
| ICEYT_6b | 1 | 50.5 | 0.7 | 15.3 | 8.4 | 0.1 | 8.4 | 13.4 | 1.6 | 0.04 | 0.01 | 1,249 | 27 | 98.6 |
| ICEYT_3 | 1 | 50.7 | 0.6 | 15.3 | 8.0 | 0.1 | 8.4 | 13.2 | 1.6 | 0.01 | 0.08 | 1,271 | bd | 98.2 |
| ICEYT_8 | 1 | 50.5 | 0.7 | 15.3 | 8.1 | 0.2 | 8.2 | 13.5 | 1.6 | 0.03 | 0.07 | 1,333 | 12 | 98.4 |
| ICEYT_7 | 1 | 51.2 | 0.7 | 15.4 | 8.2 | 0.1 | 8.1 | 13.7 | 1.6 | 0.06 | 0.06 | 1,451 | 29 | 99.2 |
| ICEYT_2a | 3 | 50.9 | 0.8 | 15.3 | 8.7 | 0.2 | 7.7 | 13.3 | 1.7 | 0.02 | 0.06 | 1,694 | 35 | 98.8 |
| ICEYT_2b | 2 | 51.2 | 0.7 | 15.3 | 8.6 | 0.2 | 7.6 | 13.6 | 1.6 | 0.09 | 0.10 | 1,809 | 29 | 99.1 |
| Spinel-hosted: | | | | | | | | | | | | | | |
| ICEYMI_3a | 1 | 50.2 | 0.8 | 16.1 | 7.9 | 0.1 | 8.8 | 13.2 | 1.6 | 0.06 | 0.02 | 1,220 | 42 | 98.9 |
| ICEYMI_3b | 1 | 49.7 | 0.7 | 15.9 | 7.7 | 0.2 | 8.7 | 13.2 | 1.8 | 0.05 | 0.05 | 1,191 | 41 | 98.1 |
| Matrix glass | | | | | | | | | | | | | | |
| ICEYT_7_gl1 | 1 | 49.2 | 1.1 | 14.8 | 9.5 | 0.2 | 8.5 | 12.9 | 1.9 | 0.25 | 0.12 | 260 | 154 | 98.5 |
| ICEYT_7_gl2 | 1 | 48.9 | 1.2 | 14.7 | 9.6 | 0.2 | 8.4 | 12.6 | 1.9 | 0.29 | 0.12 | 377 | 118 | 97.8 |
| ICEYT_7_gl3 | 1 | 49.8 | 1.2 | 15.0 | 9.3 | 0.2 | 8.2 | 12.8 | 2.0 | 0.32 | 0.18 | 385 | 117 | 98.9 |
| ICEYMI_3_gl1 | 1 | 49.0 | 1.2 | 14.6 | 9.7 | 0.2 | 8.3 | 12.6 | 2.0 | 0.28 | 0.14 | 737 | 168 | 98.3 |
| ICEYMI_3_gl2 | 1 | 48.8 | 1.1 | 14.8 | 10.0 | 0.2 | 8.5 | 12.9 | 1.8 | 0.28 | 0.16 | 521 | 176 | 98.7 |
| ICEYMI_3_gl3 | 1 | 49.4 | 1.2 | 14.6 | 9.4 | 0.2 | 8.4 | 12.9 | 2.0 | 0.32 | 0.16 | 449 | 137 | 98.7 |
| ICEYT_12_gl1 | 1 | 49.6 | 1.4 | 14.3 | 10.1 | 0.2 | 8.0 | 13.0 | 1.9 | 0.30 | 0.14 | 148 | 149 | 98.9 |
| ICEYT_12_gl2 | 1 | 49.7 | 1.4 | 14.4 | 10.1 | 0.2 | 7.9 | 13.0 | 2.0 | 0.29 | 0.16 | 181 | 152 | 99.1 |
| ICEYT_12_gl3 | 1 | 49.7 | 1.3 | 14.5 | 9.9 | 0.2 | 7.8 | 13.0 | 2.0 | 0.31 | 0.12 | 128 | 159 | 98.8 |
| ICEYT_12_gl4 | 1 | 49.8 | 1.4 | 14.7 | 10.1 | 0.2 | 8.0 | 12.6 | 2.0 | 0.28 | 0.14 | 180 | 172 | 99.2 |
| ICEYT_12_gl5 | 1 | 49.4 | 1.3 | 14.3 | 10.1 | 0.2 | 8.3 | 12.5 | 1.8 | 0.31 | 0.17 | 89 | 205 | 98.4 |
| ICEYT_3_gl | 1 | 49.0 | 1.3 | 14.8 | 9.5 | 0.2 | 8.5 | 12.9 | 2.0 | 0.28 | 0.09 | 301 | 112 | 98.5 |
| ICEYT_8_gl | 1 | 49.5 | 1.3 | 15.0 | 9.5 | 0.2 | 8.5 | 12.7 | 2.0 | 0.28 | 0.15 | 274 | 124 | 99.0 |
| G404_10_gl1 | 1 | 50.3 | 1.2 | 15.4 | 9.3 | 0.1 | 7.6 | 13.0 | 1.7 | 0.27 | 0.16 | 558 | 94 | 99.2 |
| G404_10_gl2 | 1 | 50.3 | 1.2 | 15.5 | 9.4 | 0.2 | 7.7 | 12.8 | 1.7 | 0.22 | 0.12 | 633 | 161 | 99.1 |
| G404_10_gl3 | 1 | 49.8 | 1.0 | 15.1 | 9.0 | 0.1 | 7.7 | 13.1 | 1.9 | 0.24 | 0.13 | 409 | 122 | 98.1 |
| G404_10_gl4 | 1 | 50.4 | 1.0 | 15.1 | 9.3 | 0.2 | 7.7 | 13.1 | 1.7 | 0.22 | 0.13 | 357 | 97 | 98.9 |
| G404_10_gl5 | 1 | 48.9 | 1.2 | 14.8 | 9.3 | 0.2 | 8.0 | 13.0 | 1.9 | 0.25 | 0.12 | 795 | 177 | 97.7 |
| G404_10_gl6 | 1 | 49.1 | 1.2 | 14.9 | 9.3 | 0.1 | 8.1 | 13.0 | 1.9 | 0.26 | 0.12 | 625 | 123 | 98.1 |
| G404_13_gl1 | 1 | 49.3 | 1.2 | 14.9 | 9.5 | 0.2 | 8.2 | 12.9 | 1.9 | 0.24 | 0.11 | 386 | 127 | 98.5 |
| G404_13_gl2 | 1 | 49.5 | 1.0 | 14.7 | 9.4 | 0.2 | 8.2 | 13.0 | 1.9 | 0.24 | 0.11 | 286 | 93 | 98.4 |
| G404_13_gl3 | 1 | 49.1 | 1.0 | 14.7 | 9.5 | 0.2 | 8.1 | 13.0 | 1.8 | 0.26 | 0.15 | 392 | 108 | 97.9 |
| G404_13_gl4 | 1 | 48.2 | 1.1 | 14.1 | 9.4 | 0.2 | 8.6 | 13.1 | 1.9 | 0.22 | 0.09 | 360 | 54 | 96.9 |

Table 3
Continued

| | Number of analyses | SiO ₂ | TiO ₂ | Al ₂ O ₃ | FeO | MnO | MgO | CaO | Na ₂ O | K ₂ O | P ₂ O ₅ | SO ₂ | Cl | Total |
|------------|--------------------|------------------|------------------|--------------------------------|-----|-----|-----|------|-------------------|------------------|-------------------------------|-----------------|-----|-------|
| G404_6_g11 | 1 | 49.3 | 1.0 | 14.7 | 9.3 | 0.2 | 8.3 | 12.7 | 1.9 | 0.21 | 0.13 | 521 | 126 | 97.9 |
| G404_6_g12 | 1 | 49.4 | 1.0 | 14.7 | 9.4 | 0.2 | 8.2 | 13.0 | 1.8 | 0.24 | 0.13 | 464 | 110 | 98.1 |
| G404_6_g13 | 1 | 49.1 | 1.1 | 14.6 | 9.2 | 0.2 | 8.3 | 12.6 | 1.8 | 0.25 | 0.07 | 415 | 82 | 97.2 |

Note. Uncorrected for post entrapment crystallization. Uncertainties (expressed as two standard deviation) are ± 0.3 for SiO₂, ± 0.1 for TiO₂, ± 0.2 for Al₂O₃, ± 0.07 for FeO, ± 0.05 for MnO, ± 0.09 for MgO, ± 0.2 for CaO, ± 0.2 for Na₂O, ± 0.03 for K₂O, ± 0.06 for P₂O₅, ± 115 for SO₂ and ± 58 for Cl. SO₂ and Cl are in ppm, all others are in wt.%.

Where $\delta^{13}\text{C}_{\text{melt}}$ is the $\delta^{13}\text{C}$ of C dissolved in the melt at any given point, $\delta^{13}\text{C}_{\text{initial}}$ is the initial $\delta^{13}\text{C}$ of C dissolved in the melt before any CO₂ degassing, F is the fraction of C remaining in the melt and $\alpha_{\text{gas-melt}}$ is the carbon isotopic fractionation factor between dissolved CO₂ in the melt and CO₂ in the gas phase which has recently been determined as a function of melt composition (Lee, Moussallam, Aubaud, et al., 2024; we used the average basaltic composition of melt inclusions from Halldórsson et al., 2022 and Equation 5 in Lee, Moussallam, Aubaud, et al., 2024 yielding $1,000 \ln \alpha_{\text{gas-melt}} = 2.3$). The evolution of the gas $\delta^{13}\text{C}$ can then be calculated using:

$$\delta^{13}\text{C}_{\text{gas}} = 1000 \ln \alpha_{\text{gas-melt}} + \delta^{13}\text{C}_{\text{melt}} \quad (2)$$

For open system equilibrium degassing (also called fractional equilibrium degassing or Rayleigh distillation degassing; Rayleigh, 1896), the evolution of the melt $\delta^{13}\text{C}$ is given by:

$$\delta^{13}\text{C}_{\text{initial}} = \delta^{13}\text{C}_{\text{melt}} + 1000 (1 - F^{\alpha-1}) \quad (3)$$

For closed-system kinetic degassing and open-system kinetic degassing, the evolution of the melt $\delta^{13}\text{C}$ is given by the same formula as Equations 1 and 3 respectively, except that in these cases the isotopic fractionation factor ($1000 \ln \alpha_{\text{gas-melt}}$) is replaced by the kinetic isotopic fractionation factor $1000 \ln \alpha_{\text{kinetic}}$ which, following Graham's law of diffusion, can be calculated as the square root of the inverse ratio of the molar masses of the diffusing species. This results in a kinetic isotopic fractionation factor ($1000 \ln \alpha_{\text{kinetic}}$) of -8.2% and assumes that the

Table 4
Olivine and Spinel Major Element Composition and Forsterite Content (All Measurements Taken Close to the MI)

| | Number of analyses | SiO ₂ | TiO ₂ | Al ₂ O ₃ | FeO | MnO | MgO | CaO | Cr ₂ O ₃ | NiO | Total | Fo% |
|-----------------|--------------------|------------------|------------------|--------------------------------|-------|------|------|-----|--------------------------------|------|-------|------|
| Olivine | | | | | | | | | | | | |
| G404_12 | 1 | 40.1 | 0.00 | 0.0 | 12.94 | 0.23 | 46.6 | 0.3 | 0.05 | 0.26 | 100.6 | 86.5 |
| G404_7 | 4 | 40.1 | 0.0 | 0.1 | 12.5 | 0.2 | 47.2 | 0.3 | 0.1 | 0.2 | 100.7 | 87.1 |
| ICEYT_6a | 1 | 40.7 | 0.00 | 0.0 | 12.48 | 0.18 | 47.1 | 0.3 | 0.05 | 0.28 | 101.1 | 87.1 |
| ICEYT_6b | 1 | 41.0 | 0.01 | 0.0 | 11.72 | 0.15 | 47.3 | 0.3 | 0.04 | 0.30 | 100.9 | 87.8 |
| ICEYT_3 | 1 | 41.0 | 0.0 | 0.1 | 11.7 | 0.2 | 47.8 | 0.3 | 0.1 | 0.3 | 101.4 | 87.9 |
| ICEYT_8 | 1 | 41.4 | 0.0 | 0.1 | 11.6 | 0.2 | 48.1 | 0.3 | 0.1 | 0.3 | 102.0 | 88.1 |
| ICEYT_7 | 2 | 41.0 | 0.0 | 0.1 | 11.8 | 0.2 | 47.2 | 0.3 | 0.0 | 0.2 | 100.8 | 87.7 |
| ICEYT_2a | 1 | 41.2 | 0.0 | 0.1 | 12.6 | 0.2 | 46.7 | 0.4 | 0.0 | 0.2 | 101.5 | 86.8 |
| ICEYT_2b | 1 | 41.1 | 0.00 | 0.1 | 12.59 | 0.20 | 46.5 | 0.3 | 0.03 | 0.22 | 100.9 | 86.8 |
| Cr-Spinel | | | | | | | | | | | | |
| ICEYMI_3_closea | 1 | 0.1 | 0.35 | 28.0 | 17.75 | 0.25 | 14.8 | 0.0 | 36.24 | 0.19 | 97.7 | |
| ICEYMI_3_closeb | 1 | 0.1 | 0.31 | 27.6 | 17.61 | 0.30 | 14.9 | 0.0 | 36.72 | 0.19 | 97.7 | |

Note. Errors (two standard deviations) are ± 0.2 for SiO₂, ± 0.04 for TiO₂, ± 0.03 for Al₂O₃, ± 0.1 for FeO, ± 0.04 for MnO, ± 0.04 for CaO, ± 0.1 for MgO, ± 0.02 for Cr₂O₃ and ± 0.03 NiO.

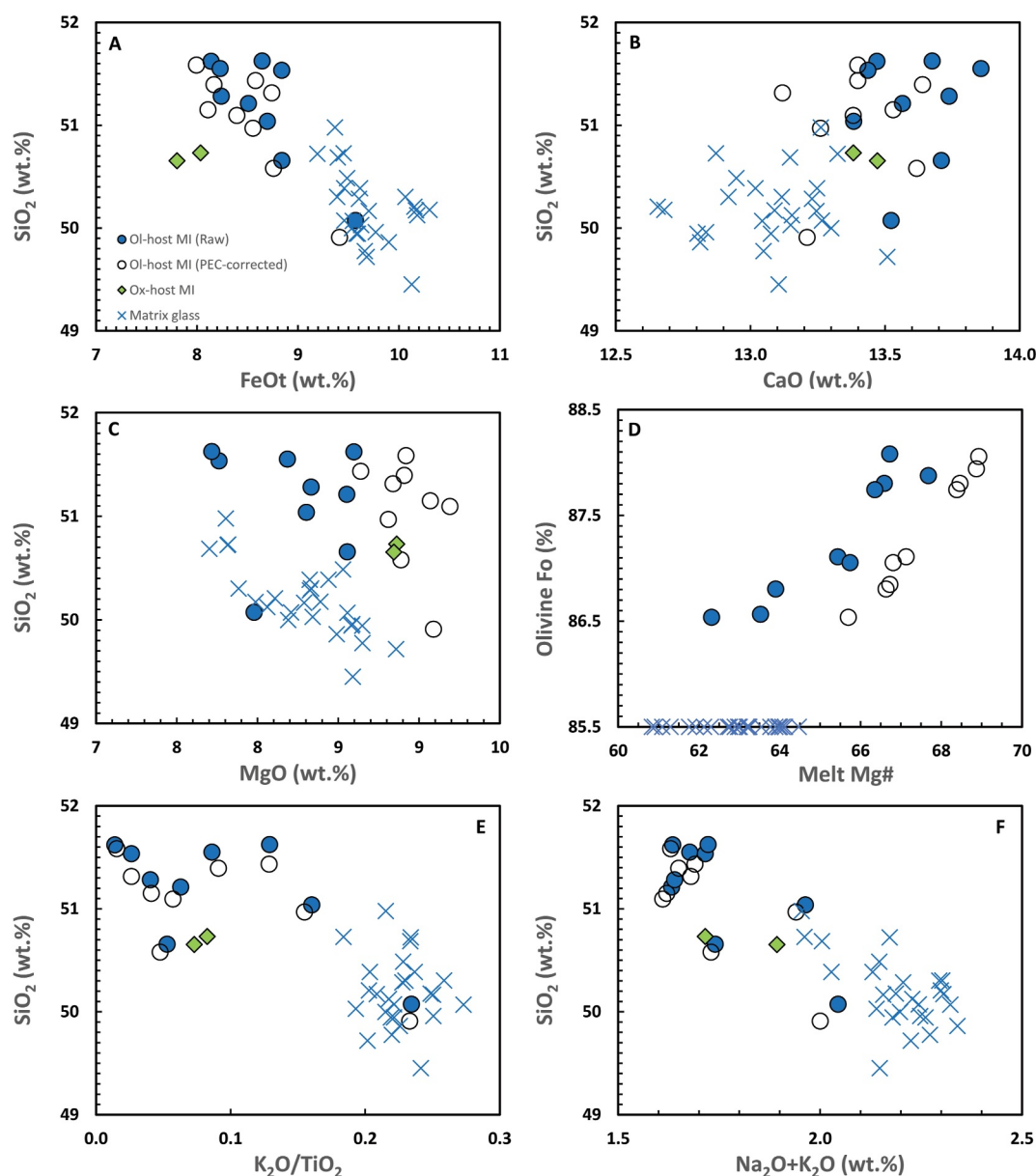


Figure 5. Major element compositions of olivine and spinel-hosted melt inclusions (olivine-hosted inclusions are shown as both PEC-corrected and raw measurements). (a) SiO₂ versus FeO_T. (b) SiO₂ versus CaO. (c) SiO₂ versus MgO. (d) Host olivine forsterite content versus melt Mg# (note that matrix glasses are arbitrarily plotted at Fo_{85.5} based on theoretical equilibrium). (e) SiO₂ versus K₂O/TiO₂. (f) SiO₂ versus Na₂O + K₂O.

diffusing species is dominantly CO₃²⁻; which is the assumption we follow or of -11.1% assuming the diffusing species is molecular CO₂.

4.2. Kinetic Isotopic Degassing During the 2021 Fagradalsfjall Eruption

Figures 6a–6d shows the evolution of $\delta^{13}\text{C}_{\text{melt}}$ and $\delta^{13}\text{C}_{\text{gas}}$ under the four possible degassing scenarios. All degassing calculations start at 1,300 ppm CO₂ and $\delta^{13}\text{C}_{\text{melt}} = -9.5\%$ (using one of the melt inclusions with the highest CO₂ content) and end when 20 ppm CO₂ remains in the melt (the average CO₂ content in matrix glasses measured by Halldórsson et al., 2022). Considering that the CO₂ content of the melt inclusions is representative of the saturation pressure, this translates to a depth range of ~ 10 km (270 MPa) to the near surface using the average melt composition from Halldórsson et al. (2022) and the saturation model of Iacono-Marziano et al. (2012). We

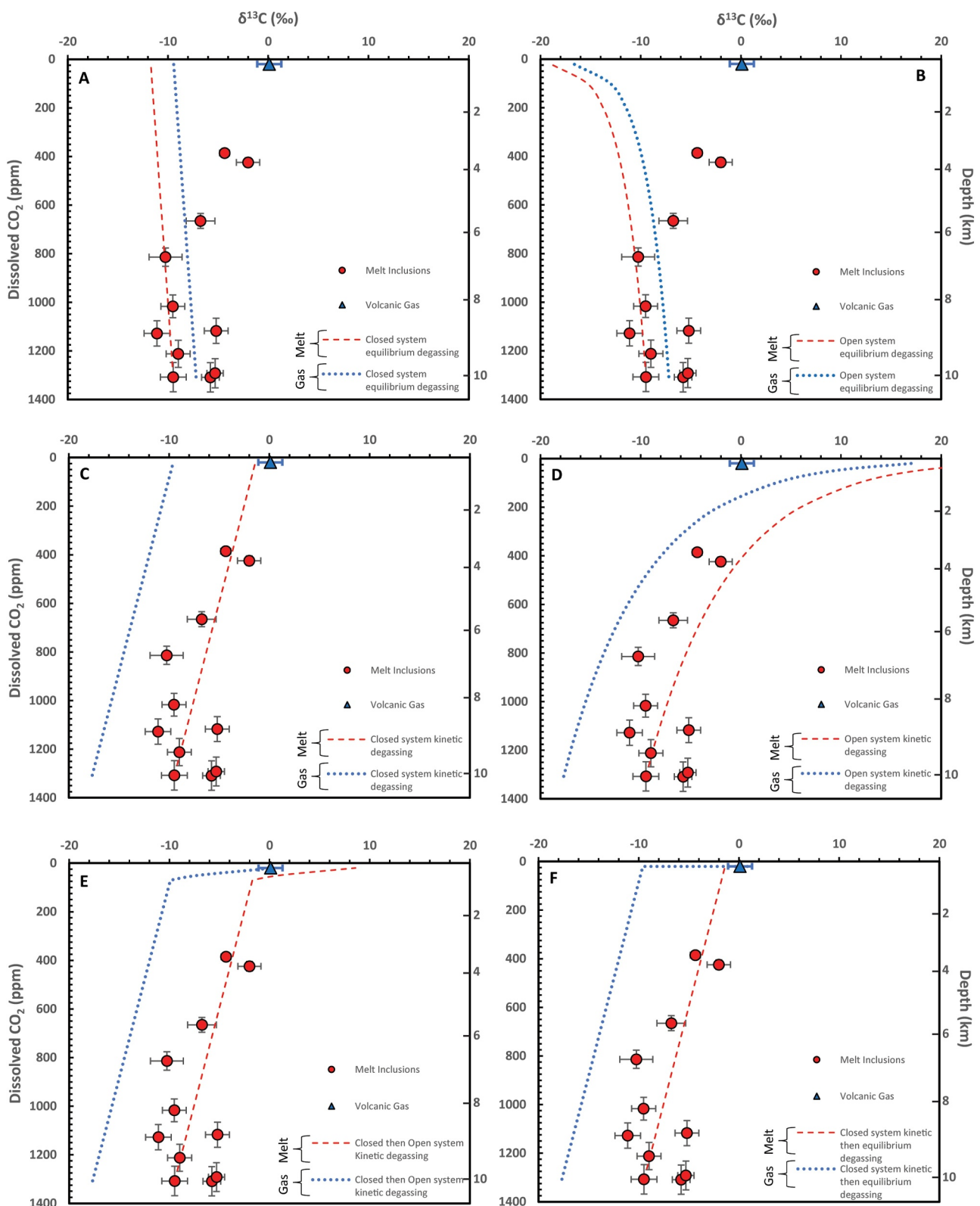


Figure 6. CO₂ content versus $\delta^{13}\text{C}$ for melt inclusions and volcanic gases from the 2021 Fagradalsfjall eruption compared to melt and gas degassing models. Depth equivalency is calculated from CO₂ content at saturation using the average melt composition from Halldórsson et al. (2022), using the solubility model of Iacono-Marziano et al. (2012) and a fixed melt density of 2.8 g/cm³.

note that this pressure/depth estimate is well within the crystallization pressure range determined by Halldórsson et al. (2022). Comparing the degassing models to our measurements, we can make several observations:

1. The equilibrium degassing scenarios, whether open or closed, both predict that $\delta^{13}\text{C}_{\text{melt}}$ should become lighter as degassing progresses, which does not reproduce the $\delta^{13}\text{C}_{\text{melt}}$ values found in the most CO_2 -poor melt inclusions (Figures 6a and 6b).
2. The kinetic degassing scenarios, whether open or closed, both predict that $\delta^{13}\text{C}_{\text{melt}}$ should become heavier as degassing progresses, reproducing the heavy $\delta^{13}\text{C}_{\text{melt}}$ values found in the most CO_2 -poor melt inclusions (Figures 6c and 6d).
3. None of the four single degassing models reproduce the $\delta^{13}\text{C}_{\text{gas}}$ values measured in the volcanic plume (Figures 6a–6d).

To reproduce both the measured $\delta^{13}\text{C}_{\text{melt}}$ and $\delta^{13}\text{C}_{\text{gas}}$ values, a two-step model is required. A closed system kinetic degassing scenario followed by an open system kinetic degassing could predict a $\delta^{13}\text{C}_{\text{gas}}$ within error of the one we measured, but this would require the transition in degassing modes to occur at a specific depth when approximately 70 ppm CO_2 remains in the melt (Figure 6e). A scenario of closed system kinetic degassing followed by equilibrium open or closed system degassing near the surface, when 20 ppm CO_2 (i.e., the matrix glass content) remains in the melt, would predict a $\delta^{13}\text{C}_{\text{gas}}$ around 0.7‰, within error of our $\delta^{13}\text{C}_{\text{gas}}$ measurements of the plume (Figure 6f). A number of other multiple-step scenarios can be drawn to reproduce both data sets, but the key point is that all would need to involve kinetic degassing for most of the degassing path. Equilibrium degassing at the surface is consistent with visual observations of the vent on our gas collection days, with passive degassing and small spattering activity. We see the scenario involving equilibrium degassing at near surface conditions (Figure 6f) therefore as the simplest and most likely. We can hypothesize that the $\delta^{13}\text{C}_{\text{gas}}$ during periods of intense fire fountaining activity might have been different (lighter) than the one we measured during passive activity.

The range in CO_2 content preserved in melt inclusions implies either that the inclusions were entrapped (and hence that their host partially grew) at a range of depth during ascent or that they re-opened and re-equilibrated at a range of depth when ascending to the surface before annealing again, or that CO_2 exsolved in a bubble. This latest scenario is unlikely since as we said earlier we only had two bubble-bearing melt inclusions. The fact that kinetic isotopic degassing of CO_2 is preserved in the melt inclusions does not necessarily imply a fast ascent rate and/or a fast olivine growth rate. In addition to magma decompression (i.e., ascent) rates, low vesicle number densities and low H_2O contents are all factors that would limit CO_2 diffusion from the melt to the gas phase (e.g., Chen, 2014; Gardner et al., 2016; Koch & Schmidt, 2023; Pichavant et al., 2013; Sierralta et al., 2002; Watson, 1991; Yoshimura, 2015; Zhang & Ni, 2010), and hence lead to kinetic isotopic fractionation. The fact that closed-system degassing with kinetic fractionation is a degassing process that has been documented in MORBs (e.g., Aubaud, 2022; Aubaud et al., 2004) which have very slow (0.002–0.2 m/s) ascent rates (e.g., Burnard, 1999; Ma et al., 2024; Moussallam et al., 2023; Sarda & Graham, 1990) further attests that a fast magma ascent and olivine growth rates are not required. For a 10 km ascent, such slow ascent rates would translate into durations of 60 days to 14 hr. Given the low water content in the 2021 Fagradalsfjall magma of less than 0.3 wt.% (Halldórsson et al., 2022), comparable to MORBs, and the estimated days to weeks period of magma mobilization and transport through the crust prior to eruption (Kahl et al., 2022; Sigmundsson et al., 2022), it is perhaps not surprising that CO_2 degassing will have been diffusion-limited for most of the ascent. Kinetic isotopic degassing might hence be a more common degassing process than previously thought, even at subaerial volcanoes.

The $\delta^{13}\text{C}$ value of volcanic gases emitted during the July 2023 eruption at Litli Hrófur, 4.5 km away from the 2021 eruption, was measured by Fischer et al. (2024). Although some samples were contaminated by moss fire, they found $\delta^{13}\text{C}$ values that extrapolate to between -9 and -5 ‰ representative of the magmatic CO_2 emitted during the eruption. Some amount of kinetic isotopic fractionation is necessary to explain the $\delta^{13}\text{C}_{\text{gas}}$ that we measured in the 2021 eruption. However, if the $\delta^{13}\text{C}_{\text{melt}}$ of our deepest melt inclusions (-10 to -6 ‰) is taken as representative of magmas across the Reykjanes Peninsula at the same depth level, then $\delta^{13}\text{C}_{\text{gas}}$ values between -9 and -5 ‰ as reported for the 2023 Litli Hrófur eruption (Fischer et al., 2024) could be reproduced by closed system degassing (equilibrium or kinetic; Figures 6a and 6c). The $\delta^{13}\text{C}$ value of hydrothermal gases in the Reykjanes Peninsula compiled by Stefánsson et al. (2017, original data therein) ranges between -5 and -3 ‰. As these are from much lower temperature fluids (260–345°C), any comparison with magmatic gases and melts would be uncertain.

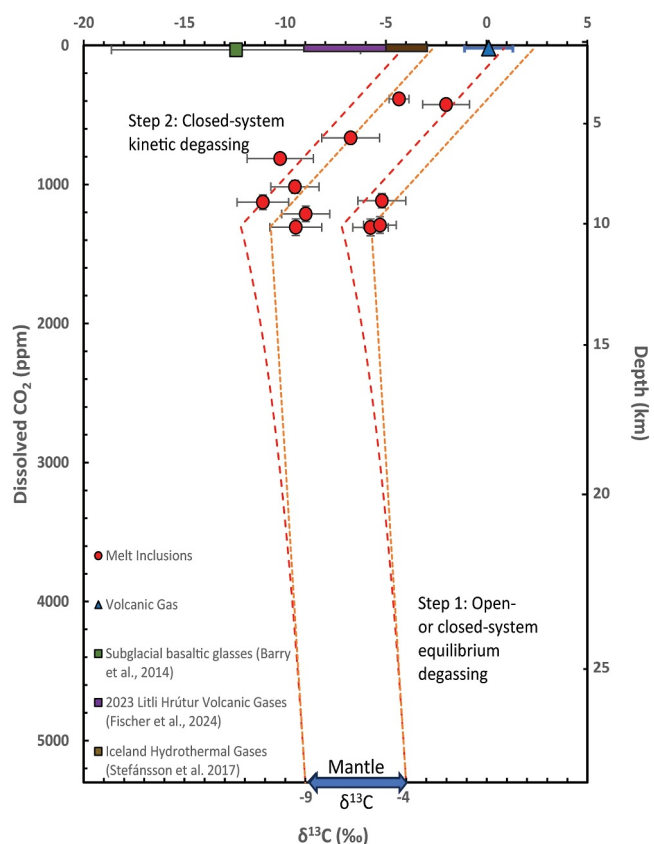


Figure 7. CO₂ content versus δ¹³C for melt inclusions (red circles) and volcanic gases (blue triangle) from the 2021 Fagradalsfjall eruption compared to melt degassing models starting at 5,300 ppm CO₂ and transitioning from equilibrium (red dashed line = open-system, orange dotted lines = closed-system) to kinetic degassing at 1,300 ppm CO₂ (all lines show closed-system kinetic degassing in step 2). An initial mantle C isotopic signature between from -4 to -9‰ can reproduce the δ¹³C range of MI. Subglacial basaltic glasses (average and standard deviation of glasses compiled over 47 localities in Iceland) from Barry et al. (2014) are also shown (green square). Their range in δ¹³C values is also consistent with an initial mantle C isotopic signature between -4 and -9‰ if equilibrium degassing only had taken place. Depth equivalency is calculated from CO₂ content at saturation using the average melt composition from Halldórsson et al. (2022), using the solubility model of Iacono-Marziano et al. (2012) and a fixed melt density of 2.8 g/cm³. The range in δ¹³C values from hydrothermal gases from the Reykjanes Peninsula (Stefánsson et al., 2017) and the range in δ¹³C values from volcanic gases during the July 2023 eruption at Litli Hrófur (Fischer et al., 2024) are also reported.

4.3. Deeper Degassing and the δ¹³C Signature of the Icelandic Mantle

Our data set only allows us to constrain degassing in the last 10 km of ascent (270 MPa saturation pressure based on the most CO₂-rich melt inclusions). However, Halldórsson et al. (2022) measured an olivine-hosted melt inclusion with 5,300 ppm CO₂ for the same 2021 eruption, indicating that the primary mantle melt must have had at least that amount of dissolved CO₂. This higher CO₂ content of the melt inclusions translates to a depth of ~27 km (755 MPa), much greater than the ~15 km thick Icelandic crust under the Reykjanes Peninsula (Weir et al., 2001). We take this 5,300 ppm CO₂ value therefore as representative of the primary CO₂ content of the melt prior to any degassing. The initial δ¹³C_{melt} at equilibrium with the Icelandic mantle underneath the Reykjanes peninsula is unknown. Assuming that the first stage of magma ascent was slow enough for CO₂ degassing to occur at isotopic equilibrium, we modeled closed- and open-system degassing for a melt starting at 5,300 ppm CO₂ followed by equilibrium kinetic degassing at 1,300 ppm CO₂ (Figure 7). We found that a mantle δ¹³C signature around -6.5 ± 2.5‰ would be able to reproduce our melt inclusion measurements. This mantle isotopic signature would also be able to reproduce the δ¹³C values (between -21‰ and -6‰) found by Barry et al. (2014) in subglacial basaltic glasses collected over a range of localities in Iceland considering equilibrium degassing only (Figure 7). We note that Barry et al. (2014), using a similar degassing model, predicted a mantle δ¹³C values of -2.5 ± 1.1‰ based on their subglacial basaltic glasses. The difference is in large part due to their use of a carbon fractionation factor between gas and melt around +4.2‰ which is not supported by the latest experimental data (Lee, Moussallam, Aubaud, et al., 2024). Our obtained mantle δ¹³C signature between -4 and -9‰ would potentially be lower than the typical -4‰ upper mantle value determined from “popping rock” samples collected at 14°N and 34°N in the Mid-Atlantic Ridge (Bekaert et al., 2023; Javoy & Pineau, 1991; Pineau et al., 2004), but would be consistent with previously reported evidence for recycled crustal material in the Icelandic mantle (Halldórsson et al., 2016) and may indicate organic carbon contamination of the Icelandic mantle. On the basis of helium isotopes, Iceland is often considered to be the most primordial hotspot on Earth (e.g., Graham et al., 1998; Hilton et al., 1999; Jackson et al., 2017). An alternative hypothesis is that the Icelandic mantle carbon isotope signature is not the result of contamination but rather preserves a primordial carbon isotopic value lower than that commonly accepted for the upper mantle. A strong limitation of our calculations is the unknown initial CO₂ content of the melt. We only have direct evidence that the initial melt CO₂ content was at least 5,300 ppm. Yet, it is entirely possible that the primary mantle melt started with even more CO₂. The equilibrium closed- and open-system degassing models can hence be extended further (i.e., deeper). If one assumed an initial melt with 1 wt.% CO₂ for instance, then a mantle δ¹³C

signature around -3 to -8‰, hence incorporating the canonical -4‰ upper mantle value, would be able to reproduce our melt inclusion measurements.

4.4. A Heterogeneous δ¹³C Signature for the Icelandic Mantle

Our discussion so far has assumed that the eruption of Fagradalsfjall erupted magmas sourced from a partial melting of a mantle region that is homogeneous in its δ¹³C signature. As previously noted by Halldórsson et al. (2022), however, the geochemical variety preserved in the 2021 erupted products, such as the range in K₂O/TiO₂, points to melt contributions from a variety of mantle sources. Halldórsson et al. (2022) interpreted this chemical heterogeneity as the result of mixing between a shallow mantle source producing more depleted melts at a higher melt fraction and a deeper mantle source producing more enriched melts at a smaller melt fraction. Our

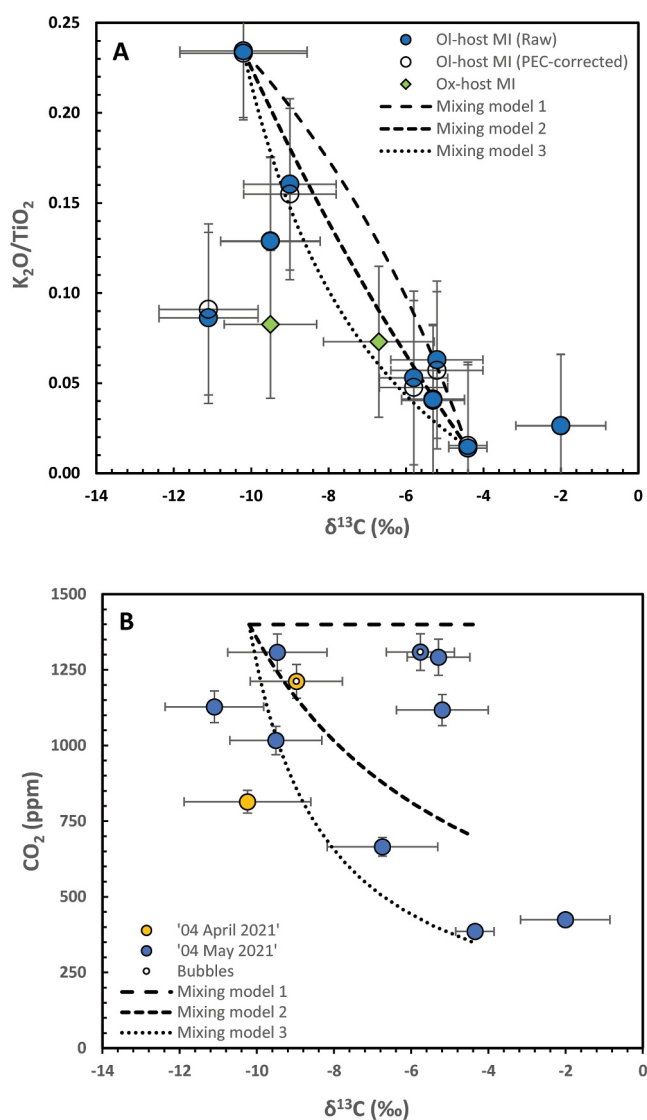


Figure 8. (a) K_2O/TiO_2 Ratio versus $\delta^{13}C$ for melt inclusions and theoretical mixing lines (see text for details). (b) CO_2 content versus $\delta^{13}C$ for melt inclusions and theoretical mixing lines.

melt inclusions record the same geochemical variety identified by Halldórs-son et al. (2022) with K_2O/TiO_2 ratios between 0.01 and 0.23. Taking these two extreme values as magmatic endmembers, we can calculate theoretical mixing lines. Figure 8 shows three such mixing models overlaid on the melt inclusion data. The first mixing model assumes that both magmas have similar CO_2 contents (arbitrarily fixed at 1,400 ppm). The second and third mixing models assume that the low K_2O/TiO_2 ratio magma has a CO_2 content half (700 ppm) or one fourth (350 ppm) that of the high K_2O/TiO_2 magma. None of these models does an amazing job at reproducing the data, but the general trendlines they predict are broadly consistent with the observations. The main discrepancy of such a mixing model, however, arises when we consider the gas phase. The $\delta^{13}C_{gas}$ we measured is $+0.1 \pm 1.2\text{‰}$. The $\delta^{13}C_{melt}$ at equilibrium with such a gas should be around -2‰ . Yet all our glass analyses show high K_2O/TiO_2 ratios around 0.23, which, following the mixing hypothesis, should have $\delta^{13}C_{melt}$ around -10‰ (i.e., the glasses would be expected to plot in the top right corner in Figure 8a). Unless we postulate that the gas phase is unrelated to the melt that makes the bulk of the matrix glass composition, the measured $\delta^{13}C_{gas}$ is irreconcilable with a magma mixing scenario and a degassing model, necessarily involving kinetic degassing, is still needed to explain it. Although we have treated the degassing and magma mixing hypotheses as separate, there is no reason why both could not have occurred simultaneously to some extent. A heterogeneous $\delta^{13}C$ value of the mantle source (between -4 and -9‰) of two magmas mixing in the plumbing system helps explain the spread in $\delta^{13}C$ measured in melt inclusions with similar CO_2 contents (Figure 7), while isotopic fractionation due to CO_2 degassing helps reconcile the spread in $\delta^{13}C$ measured in melt inclusions with similar K_2O/TiO_2 ratios (Figure 8) and is necessary to reconcile the $\delta^{13}C_{gas}$ measurements.

5. Conclusions

In this study, we investigated the carbon stable isotope evolution of the melt and gas phases during the 2021 eruption of Fagradalsfjall. We present $\delta^{13}C$ measurements in CO_2 gas from volcanic gases collected by UAS directly above the erupting vent. We also present $\delta^{13}C$ measurements in mineral-hosted melt inclusions (i.e., dissolved CO_2) from the same eruptive event. Our results provide evidence for closed-system kinetic degassing of CO_2 during magma ascent, followed by equilibrium and/or open-system degassing near the surface. This degassing behavior, previously identified primarily in mid-ocean ridge basalts, sheds light on the dynamics of CO_2 exsolution

during volcanic eruptions. Our results suggest that kinetic isotopic degassing may be a more common process than previously thought, even in subaerial volcanic environments. The large changes in $\delta^{13}C$ recorded in the melt during degassing, and the discrepancies between the measured isotopic signatures of volcanic gases and those predicted by simple degassing models, highlight the limitations of using $\delta^{13}C$ in volcanic gases alone to infer C origin in the mantle source. Instead, our results underscore the importance of using a combined approach measuring gas and melt inclusions to accurately interpret the complex degassing mechanisms during volcanic eruptions. Finally, we constrain the C isotopic signature of the mantle beneath the Reykjanes Peninsula to a value of $-6.5 \pm 2.5\text{‰}$, but show that local heterogeneity in mantle $\delta^{13}C$ may exist, suggesting a possible spatially dependent organic carbon contamination of the Icelandic mantle.

Data Availability Statement

Supplementary figures and tables are archived via Moussallam (2024).

Acknowledgments

We thank Nordine Bouden and Johan Villeneuve for their invaluable support during the SIMS analyses at CRPG-CNRS Nancy lab, France. We thank Einat Lev at the Lamont Doherty Earth Observatory for allowing use of the DJI Matrice 210.

References

- Allard, P. (1979). $^{13}\text{C}/^{12}\text{C}$ and $^{34}\text{S}/^{32}\text{S}$ ratios in magmatic gases from ridge volcanism in Afar. *Nature*, 282(5734), 56–58. <https://doi.org/10.1038/282056a0>
- Allard, P., Le Guern, F., & Sabroux, J. C. (1977). Thermodynamic and isotopic studies in eruptive gases. *Geothermics*, 5(1–4), 37–40. [https://doi.org/10.1016/0375-6505\(77\)90006-2](https://doi.org/10.1016/0375-6505(77)90006-2)
- Aubaud, C. (2022). Carbon stable isotope constraints on CO_2 degassing models of ridge, hotspot and arc magmas. *Chemical Geology*, 605, 120962. <https://doi.org/10.1016/j.chemgeo.2022.120962>
- Aubaud, C., Pineau, F., Hékinian, R., & Javoy, M. (2005). Degassing of CO_2 and H_2O in submarine lavas from the Society hotspot. *Earth and Planetary Science Letters*, 235(3–4), 511–527. <https://doi.org/10.1016/j.epsl.2005.04.047>
- Aubaud, C., Pineau, F., Hékinian, R., & Javoy, M. (2006). Carbon and hydrogen isotope constraints on degassing of CO_2 and H_2O in submarine lavas from the Pitcairn hotspot (South Pacific). *Geophysical Research Letters*, 33(2). <https://doi.org/10.1029/2005GL024907>
- Aubaud, C., Pineau, F., Jambon, A., & Javoy, M. (2004). Kinetic disequilibrium of C, He, Ar and carbon isotopes during degassing of mid-ocean ridge basalts. *Earth and Planetary Science Letters*, 222(2), 391–406. <https://doi.org/10.1016/j.epsl.2004.03.001>
- Barnie, T., Hjörvar, T., Titos, M., Sigurðsson, E. M., Pálsson, S. K., Bergsson, B., et al. (2023). Volcanic plume height monitoring using calibrated web cameras at the Icelandic meteorological office: System overview and first application during the 2021 Fagradalsfjall eruption. *Journal of Applied Volcanology*, 12(1), 4. <https://doi.org/10.1186/s13617-023-00130-9>
- Barry, P. H., Hilton, D. R., Füre, E., Halldórrsson, S. A., & Grönvold, K. (2014). Carbon isotope and abundance systematics of Icelandic geothermal gases, fluids and subglacial basalts with implications for mantle plume-related CO_2 fluxes. *Geochimica et Cosmochimica Acta*, 134, 74–99. <https://doi.org/10.1016/j.gca.2014.02.038>
- Barsotti, S., Parks, M. M., Pfeffer, M. A., Óladóttir, B. A., Barnie, T., Titos, M. M., et al. (2023). The eruption in Fagradalsfjall (2021, Iceland): How the operational monitoring and the volcanic hazard assessment contributed to its safe access. *Natural Hazards*, 116(3), 3063–3092. <https://doi.org/10.1007/s11069-022-05798-7>
- Bekaert, D. V., Barry, P. H., Curtice, J., Blusztajn, J., Hudak, M., Seltzer, A., et al. (2023). A carbon, nitrogen, and multi-isotope study of basalt glasses near 14°N on the Mid-Atlantic Ridge. Part A: Degassing processes. *Geochimica et Cosmochimica Acta*, 369, 160–178. <https://doi.org/10.1016/j.gca.2023.12.015>
- Brown, P. E., Bowman, J. R., & Kelly, W. C. (1985). Petrologic and stable isotope constraints on the source and evolution of skarn-forming fluids at Pine Creek, California. *Economic Geology*, 80(1), 72–95. <https://doi.org/10.2113/gsecongeo.80.1.72>
- Burnard, P. (1999). Eruption dynamics of “popping rock” from vesicle morphologies. *Journal of Volcanology and Geothermal Research*, 92(3–4), 247–258. [https://doi.org/10.1016/s0377-0273\(99\)00057-8](https://doi.org/10.1016/s0377-0273(99)00057-8)
- Capasso, G., Carapezza, M. L., Federico, C., Inguaggiato, S., & Rizzo, A. (2005). Geochemical monitoring of the 2002–2003 eruption at Stromboli volcano (Italy): Precursory changes in the carbon and helium isotopic composition of fumarole gases and thermal waters. *Bulletin of Volcanology*, 68(2), 118–134. <https://doi.org/10.1007/s00445-005-0427-5>
- Cartigny, P., Jendrzewski, N., Pineau, F., Petit, E., & Javoy, M. (2001). Volatile (C, N, Ar) variability in MORB and the respective roles of mantle source heterogeneity and degassing: The case of the southwest Indian ridge. *Earth and Planetary Science Letters*, 194(1–2), 241–257. [https://doi.org/10.1016/S0012-821X\(01\)00540-4](https://doi.org/10.1016/S0012-821X(01)00540-4)
- Chen, X. (2014). CO_2 diffusion in dry and hydrous haplobasaltic melts.
- Chiodini, G., Caliro, S., Aiuppa, A., Avino, R., Granieri, D., Moretti, R., & Parello, F. (2011). First C-13/C-12 isotopic characterisation of volcanic plume CO_2 . *Bulletin of Volcanology*, 73(5), 531–542. <https://doi.org/10.1007/s00445-010-0423-2>
- Danyushevsky, L. V., Della-Pasqua, F. N., & Sokolov, S. (2000). Re-equilibration of melt inclusions trapped by magnesium olivine phenocrysts from subduction-related magmas: Petrological implications. *Contributions to Mineralogy and Petrology*, 138(1), 68–83. <https://doi.org/10.1007/PL00007664>
- Danyushevsky, L. V., & Plechov, P. (2011). Petrolog3: Integrated software for modeling crystallization processes. *Geochemistry, Geophysics, Geosystems*, 12(7). <https://doi.org/10.1029/2011GC003516>
- D’Arcey, F., de Moor, J. M., Stix, J., Alan, A., Bogue, R., Corrales, E., et al. (2022). New insights into carbon isotope systematics at Poás volcano, Costa Rica. *Journal of Volcanology and Geothermal Research*, 431, 107639. <https://doi.org/10.1016/j.jvolgeores.2022.107639>
- Des Marais, D. J., & Moore, J. G. (1984). Carbon and its isotopes in mid-oceanic basaltic glasses. *Earth and Planetary Science Letters*, 69(1), 43–57. [https://doi.org/10.1016/0012-821X\(84\)90073-6](https://doi.org/10.1016/0012-821X(84)90073-6)
- Fischer, T. P., & Lopez, T. M. (2016). First airborne samples of a volcanic plume for $\delta^{13}\text{C}$ of CO_2 determinations. *Geophysical Research Letters*, 43(7), 2016GL068499. <https://doi.org/10.1002/2016GL068499>
- Fischer, T. P., Mandon, C. L., Nowicki, S., Ericksen, J., Vilches, F. R., Pfeffer, M. A., et al. (2024). CO_2 emissions during the 2023 Litli Hrutur eruption in Reykjanes, Iceland: $\delta^{13}\text{C}$ tracks magma degassing. *Bulletin of Volcanology*, 86(6), 60. <https://doi.org/10.1007/s00445-024-01751-7>
- Galle, B., Arellano, S., Bobrowski, N., Conde, V., Fischer, T. P., Gerdes, G., et al. (2021). A multi-purpose, multi-rotor drone system for long-range and high-altitude volcanic gas plume measurements. *Atmospheric Measurement Techniques*, 14(6), 4255–4277. <https://doi.org/10.5194/amt-14-4255-2021>
- Gardner, J. E., Jackson, B. A., Gonnermann, H., & Soule, S. A. (2016). Rapid ascent and emplacement of basaltic lava during the 2005–06 eruption of the East Pacific Rise at ca. $9^\circ 51'\text{N}$ as inferred from CO_2 contents. *Earth and Planetary Science Letters*, 453, 152–160. <https://doi.org/10.1016/j.epsl.2016.08.007>
- Gerlach, T. M., & Taylor, B. E. (1990). Carbon isotope constraints on degassing of carbon dioxide from Kilauea Volcano. *Geochimica et Cosmochimica Acta*, 54(7), 2051–2058. [https://doi.org/10.1016/0016-7037\(90\)90270-U](https://doi.org/10.1016/0016-7037(90)90270-U)
- Graham, D. W., Larsen, L. M., Hanan, B. B., Storey, M., Pedersen, A. K., & Lupton, J. E. (1998). Helium isotope composition of the early Iceland mantle plume inferred from the Tertiary picrites of West Greenland. *Earth and Planetary Science Letters*, 160(3–4), 241–255. [https://doi.org/10.1016/S0012-821X\(98\)00083-1](https://doi.org/10.1016/S0012-821X(98)00083-1)
- Halldórrsson, S. A., Hilton, D. R., Barry, P. H., Füre, E., & Grönvold, K. (2016). Recycling of crustal material by the Iceland mantle plume: New evidence from nitrogen elemental and isotope systematics of subglacial basalts. *Geochimica et Cosmochimica Acta*, 176, 206–226. <https://doi.org/10.1016/j.gca.2015.12.021>

- Halldórsson, S. A., Marshall, E. W., Caracciolo, A., Matthews, S., Bali, E., Rasmussen, M. B., et al. (2022). Rapid shifting of a deep magmatic source at Fagradalsfjall volcano, Iceland. *Nature*, *609*(7927), 529–534. <https://doi.org/10.1038/s41586-022-04981-x>
- Hilton, D. R., Grönvold, K., Macpherson, C. G., & Castillo, P. R. (1999). Extreme $^3\text{He}/^4\text{He}$ ratios in northwest Iceland: Constraining the common component in mantle plumes. *Earth and Planetary Science Letters*, *173*(1–2), 53–60. [https://doi.org/10.1016/s0012-821x\(99\)00215-0](https://doi.org/10.1016/s0012-821x(99)00215-0)
- Hilton, D. R., Ramirez, C. J., Mora-Amador, R., Fischer, T. P., Fueri, E., Barry, P. H., & Shaw, A. M. (2010). Monitoring of temporal and spatial variations in fumarole helium and carbon dioxide characteristics at Poas and Turrialba volcanoes, Costa Rica (2001–2009). *Geochemical Journal*, *44*, 431–440.
- Iacono-Marziano, G., Morizet, Y., Le Trong, E., & Gaillard, F. (2012). New experimental data and semi-empirical parameterization of H_2O – CO_2 solubility in mafic melts. *Geochimica et Cosmochimica Acta*, *97*, 1–23. <https://doi.org/10.1016/j.gca.2012.08.035>
- Jackson, M. G., Konter, J. G., & Becker, T. W. (2017). Primordial helium entrained by the hottest mantle plumes. *Nature*, *542*(7641), 340–343. <https://doi.org/10.1038/nature21023>
- Javoy, M., & Pineau, F. (1991). The volatiles record of a “popping” rock from the mid-Atlantic ridge at 14°N : Chemical and isotopic composition of gas trapped in the vesicles. *Earth and Planetary Science Letters*, *107*(3–4), 598–611. [https://doi.org/10.1016/0012-821X\(91\)90104-P](https://doi.org/10.1016/0012-821X(91)90104-P)
- Jendrzewski, N. (1994). *Relations entre dynamique d'éruption et géochimie élémentaire et isotopique du carbone et de l'eau dans les basaltes de rides* (These de doctorat). Institut de physique du globe.1921.
- Kahl, M., Mutch, E. J. F., MacLennan, J., Morgan, D. J., Couperthwaite, F., Bali, E., et al. (2022). Deep magma mobilization years before the 2021 CE Fagradalsfjall eruption, Iceland. *Geology*, *51*(2), 184–188. <https://doi.org/10.1130/G50340.1>
- Keeling, C. D. (1958). The concentration and isotopic abundances of atmospheric carbon dioxide in rural areas. *Geochimica et Cosmochimica Acta*, *13*(4), 322–334. [https://doi.org/10.1016/0016-7037\(58\)90033-4](https://doi.org/10.1016/0016-7037(58)90033-4)
- Koch, L., & Schmidt, B. C. (2023). CO_2 diffusion in dry and hydrous leucititic melt. *European Journal of Mineralogy*, *35*(1), 117–132. <https://doi.org/10.5194/ejm-35-117-2023>
- Kress, V. C., & Carmichael, I. S. E. (1988). Stoichiometry of the iron oxidation reaction in silicate melts. *American Mineralogist*, *73*, 1267–1274.
- Lange, R. A., & Carmichael, I. S. E. (1987). Densities of Na_2O – K_2O – CaO – MgO – FeO – Fe_2O_3 – Al_2O_3 – TiO_2 – SiO_2 liquids: New measurements and derived partial molar properties. *Geochimica et Cosmochimica Acta*, *51*(11), 2931–2946. [https://doi.org/10.1016/0016-7037\(87\)90368-1](https://doi.org/10.1016/0016-7037(87)90368-1)
- Lee, H., Moussallam, Y., Aubaud, C., Iacono-Marziano, G., Hammond, K., & Ebel, D. (2024). Carbon isotope fractionation between CO_2 and carbon in silicate melts at high temperature. *Geochimica et Cosmochimica Acta*, *380*, 208–219. <https://doi.org/10.1016/j.gca.2024.07.015>
- Lee, H. J., Moussallam, Y., Rose-Koga, E., Piani, L., Villeneuve, J., Bouden, N., et al. (2024b). High-precision determination of carbon stable isotope in silicate glasses by secondary ion mass spectrometry: Evaluation of international standards. *Chemical Geology*, *122428*. <https://doi.org/10.1016/j.chemgeo.2024.122428>
- Liu, E. J., Aiuppa, A., Alan, A., Arellano, S., Bitetto, M., Bobrowski, N., et al. (2020). Aerial strategies advance volcanic gas measurements at inaccessible, strongly degassing volcanoes. *Science Advances*, *6*(44), eabb9103. <https://doi.org/10.1126/sciadv.abb9103>
- Ma, B., Liu, P.-P., Dick, H. J. B., Zhou, M.-F., Chen, Q., & Liu, C.-Z. (2024). Trans-lithospheric ascent processes of the deep-rooted magma plumbing system underneath the ultraslow-spreading SW Indian ridge. *Journal of Geophysical Research: Solid Earth*, *129*(1), e2023JB027224. <https://doi.org/10.1029/2023JB027224>
- Macpherson, C., & Matthey, D. (1994). Carbon isotope variations of CO_2 in Central Lau Basin basalts and ferrobasalts. *Earth and Planetary Science Letters*, *121*(3–4), 263–276. [https://doi.org/10.1016/0012-821X\(94\)90072-8](https://doi.org/10.1016/0012-821X(94)90072-8)
- Macpherson, C. G., Hilton, D. R., & Hammerschmidt, K. (2010). No slab-derived CO_2 in Mariana Trough back-arc basalts: Implications for carbon subduction and for temporary storage of CO_2 beneath slow spreading ridges. *Geochemistry, Geophysics, Geosystems*, *11*. <https://doi.org/10.1029/2010GC003293>
- Malowany, K. S., Stix, J., de Moor, J. M., Chu, K., Lacrampe-Couloume, G., & Sherwood Lollar, B. (2017). Carbon isotope systematics of Turrialba volcano, Costa Rica, using a portable cavity ring-down spectrometer. *Geochemistry, Geophysics, Geosystems*, *18*(7), 2769–2784. <https://doi.org/10.1002/2017GC006856>
- Marty, B., & Jambon, A. (1987). C_3H_8 in volatile fluxes from the solid Earth: Implications for carbon geodynamics. *Earth and Planetary Science Letters*, *83*(1–4), 16–26. [https://doi.org/10.1016/0012-821X\(87\)90047-1](https://doi.org/10.1016/0012-821X(87)90047-1)
- Moore, J. G., Batchelder, J. N., & Cunningham, C. G. (1977). CO_2 -filled vesicles in mid-ocean basalt. *Journal of Volcanology and Geothermal Research*, *2*(4), 309–327. [https://doi.org/10.1016/0377-0273\(77\)90018-X](https://doi.org/10.1016/0377-0273(77)90018-X)
- Moussallam, Y. (2024). Supplementary figures and tables to Kinetic isotopic degassing of CO_2 during the 2021 Fagradalsfjall eruption and the $\delta^{13}\text{C}$ signature of the Icelandic mantle [Dataset]. *figshare*. <https://doi.org/10.6084/m9.figshare.25723059.v2>
- Moussallam, Y., Georgeais, G., Rose-Koga, E. F., Koga, K. T., Hartley, M. E., Scaillet, B., et al. (2023). CO_2 -Undersaturated melt inclusions from the south west Indian ridge record surprisingly uniform redox conditions. *Geochemistry, Geophysics, Geosystems*, *24*(12), e2023GC011235. <https://doi.org/10.1029/2023GC011235>
- Obase, T., Sumino, H., Toyama, K., Kawana, K., Yamane, K., Yaguchi, M., et al. (2022). Monitoring of magmatic–hydrothermal system by noble gas and carbon isotopic compositions of fumarolic gases. *Scientific Reports*, *12*(1), 17967. <https://doi.org/10.1038/s41598-022-22280-3>
- Pedersen, G. B. M., Belart, J. M. C., Óskarsson, B. V., Gudmundsson, M. T., Gies, N., Högnadóttir, T., et al. (2022). Volume, effusion rate, and Lava transport during the 2021 Fagradalsfjall eruption: Results from near real-time photogrammetric monitoring. *Geophysical Research Letters*, *49*(13), e2021GL097125. <https://doi.org/10.1029/2021GL097125>
- Pichavant, M., Carlo, I. D., Rotolo, S. G., Scaillet, B., Burgisser, A., Gall, N. L., & Martel, C. (2013). Generation of CO_2 -rich melts during basalt magma ascent and degassing. *Contributions to Mineralogy and Petrology*, *166*(2), 545–561. <https://doi.org/10.1007/s00410-013-0890-5>
- Pineau, F., & Javoy, M. (1983). Carbon isotopes and concentrations in mid-oceanic ridge basalts. *Earth and Planetary Science Letters*, *62*(2), 239–257. [https://doi.org/10.1016/0012-821X\(83\)90087-0](https://doi.org/10.1016/0012-821X(83)90087-0)
- Pineau, F., & Javoy, M. (1994). Strong degassing at ridge crests: The behaviour of dissolved carbon and water in basalt glasses at 14°N , Mid-Atlantic Ridge. *Earth and Planetary Science Letters*, *123*(1–3), 179–198. [https://doi.org/10.1016/0012-821X\(94\)90266-6](https://doi.org/10.1016/0012-821X(94)90266-6)
- Pineau, F., Javoy, M., & Bottinga, Y. (1976). $^{13}\text{C}/^{12}\text{C}$ ratios of rocks and inclusions in popping rocks of the Mid-Atlantic Ridge and their bearing on the problem of isotopic composition of deep-seated carbon. *Earth and Planetary Science Letters*, *29*(2), 413–421. [https://doi.org/10.1016/0012-821X\(76\)90146-1](https://doi.org/10.1016/0012-821X(76)90146-1)
- Pineau, F., Shilobreeva, S., Hekinian, R., Bideau, D., & Javoy, M. (2004). Deep-sea explosive activity on the mid-Atlantic ridge near $34^\circ50'\text{N}$: A stable isotope (C, H, O) study. *Chemical Geology*, *211*(1–2), 159–175. <https://doi.org/10.1016/j.chemgeo.2004.06.029>
- Rayleigh, L. (1896). L. Theoretical considerations respecting the separation of gases by diffusion and similar processes. *The London, Edinburgh and Dublin Philosophical Magazine and Journal of Science*, *42*(259), 493–498. <https://doi.org/10.1080/14786449608620944>
- Rizzo, A. L., Jost, H.-J., Caracausi, A., Paonita, A., Liotta, M., & Martelli, M. (2014). Real-time measurements of the concentration and isotope composition of atmospheric and volcanic CO_2 at Mount Etna (Italy). *Geophysical Research Letters*, *41*(7), 2014GL059722. <https://doi.org/10.1002/2014GL059722>

- Rizzo, A. L., Liuzzo, M., Ancellin, M. A., & Jost, H. J. (2015). Real-time measurements of $\delta^{13}\text{C}$, CO_2 concentration, and CO_2/SO_2 in volcanic plume gases at Mount Etna, Italy, over 5 consecutive days. *Chemical Geology*, *411*, 182–191. <https://doi.org/10.1016/j.chemgeo.2015.07.007>
- Sano, Y., & Marty, B. (1995). Origin of carbon in fumarolic gas from island arcs. *Chemical Geology*, *119*(1–4), 265–274. [https://doi.org/10.1016/0009-2541\(94\)00097-R](https://doi.org/10.1016/0009-2541(94)00097-R)
- Sano, Y., & Williams, S. N. (1996). Fluxes of mantle and subducted carbon along convergent plate boundaries. *Geophysical Research Letters*, *23*(20), 2749–2752. <https://doi.org/10.1029/96GL02260>
- Sarda, P., & Graham, D. (1990). Mid-ocean ridge popping rocks: Implications for degassing at ridge crests. *Earth and Planetary Science Letters*, *97*(3–4), 268–289. [https://doi.org/10.1016/0012-821x\(90\)90047-2](https://doi.org/10.1016/0012-821x(90)90047-2)
- Sato, M., Mori, T., Shimoike, Y., Nagao, K., & Notsu, K. (2002). Carbon isotope systematics of CO_2 , CO and CH_4 in fumarolic gases from Satsuma-Iwojima volcanic island, Japan. *Earth Planets and Space*, *54*(3), 257–263. <https://doi.org/10.1186/BF03353025>
- Schipper, C. I., Moussallam, Y., Curtis, A., Peters, N., Barnie, T., Bani, P., et al. (2017). Isotopically ($\delta^{13}\text{C}$ and $\delta^{18}\text{O}$) heavy volcanic plumes from Central Andean volcanoes: A field study. *Bulletin of Volcanology*, *79*(8), 65. <https://doi.org/10.1007/s00445-017-1146-4>
- Scott, S., Pfeffer, M., Oppenheimer, C., Bali, E., Lamb, O. D., Barnie, T., et al. (2023). Near-surface magma flow instability drives cyclic lava fountaining at Fagradalsfjall, Iceland. *Nature Communications*, *14*(1), 6810. <https://doi.org/10.1038/s41467-023-42569-9>
- Sierralta, M., Nowak, M., & Keppler, H. (2002). The influence of bulk composition on the diffusivity of carbon dioxide in Na aluminosilicate melts. *American Mineralogist*, *87*(11–12), 1710–1716. <https://doi.org/10.2138/am-2002-11-1221>
- Sigmundsson, F., Parks, M., Hooper, A., Geirsson, H., Vogfjörð, K. S., Drouin, V., et al. (2022). Deformation and seismicity decline before the 2021 Fagradalsfjall eruption. *Nature*, *609*(7927), 523–528. <https://doi.org/10.1038/s41586-022-05083-4>
- Stefánsson, A., Hilton, D. R., Sveinbjörnsdóttir, Á. E., Torssander, P., Heinemeier, J., Barnes, J. D., et al. (2017). Isotope systematics of Icelandic thermal fluids. *Journal of Volcanology and Geothermal Research*, *337*, 146–164. <https://doi.org/10.1016/j.jvolgeores.2017.02.006>
- Toplis, M. J. (2005). The thermodynamics of iron and magnesium partitioning between olivine and liquid: Criteria for assessing and predicting equilibrium in natural and experimental systems. *Contributions to Mineralogy and Petrology*, *149*(1), 22–39. <https://doi.org/10.1007/s00410-004-0629-4>
- Varekamp, J. C., Kreulen, R., Poorter, R. P. E., & Van Bergen, M. J. (1992). Carbon sources in arc volcanism, with implications for the carbon cycle. *Terra Nova*, *4*(3), 363–373. <https://doi.org/10.1111/j.1365-3121.1992.tb00825.x>
- Watson, B. (1991). Diffusion of dissolved CO_2 and Cl in hydrous silicic to intermediate magmas. *Geochimica et Cosmochimica Acta*, *55*(7), 1897–1902. [https://doi.org/10.1016/0016-7037\(91\)90031-Y](https://doi.org/10.1016/0016-7037(91)90031-Y)
- Weir, N. R. W., White, R. S., Brandsdóttir, B., Einarsson, P., Shimamura, H., & Shiobara, H. (2001). Crustal structure of the northern Reykjanes ridge and Reykjanes Peninsula, southwest Iceland. *Journal of Geophysical Research*, *106*(B4), 6347–6368. <https://doi.org/10.1029/2000JB900358>
- Yoshimura, S. (2015). Diffusive fractionation of H_2O and CO_2 during magma degassing. *Chemical Geology*, *411*, 172–181. <https://doi.org/10.1016/j.chemgeo.2015.07.003>
- Zhang, Y., & Ni, H. (2010). Diffusion of H, C, and O components in silicate melts. *Reviews in Mineralogy and Geochemistry*, *72*(1), 171–225. <https://doi.org/10.2138/rmg.2010.72.5>